GEORGIA DOT RESEARCH PROJECT 22-19

Final Report

REMOTE BRIDGE HEALTH MONITORING FOR SCOURING USING COST-EFFICIENT SENSING TECHNOLOGY

Office of Performance-based Management and Research
600 West Peachtree Street NW | Atlanta, GA 30308

November 2025

TECHNICAL REPORT DOCUMENTATION PAGE

1. Report No. FHWA-GA-25-2219	**2. Government Accession No.** N/A	**3. Recipient's Catalog No.** N/A
4. Title and Subtitle Remote Bridge Health Monitoring for Scouring Using Cost-Efficient Sensing Technology		**5. Report Date** November 2025 **6. Performing Organization Code** N/A
7. Author(s) Tien Yee (PI), Ph.D., Jidong J. Yang (Co-PI), Ph.D., P.E., FITE, Metin Oguzmert (Co-PI), Ph.D., P.E., S.E, Mahyar Amirgholy (Co-PI), Ph.D., Alan Kazemian, Ph.D, Research Assistant, Ajoy Sarkar, Research Assistant, Md. Shamsul Alam, Research Assistant, Penghao Deng, Research Assistant		**8. Performing Organization Report No.** 22-19
9. Performing Organization Name and Address Kennesaw State University Southern Polytechnic College of Engineering and Engineering Technology Marietta, GA 30060 Phone: (470)578-5091, Email: tyee@kennesaw.edu		**10. Work Unit No.** N/A **11. Contract or Grant No.** #0019322
12. Sponsoring Agency Name and Address Georgia Department of Transportation Office of Transportation Data 600 West Peachtree Street NW Atlanta, GA 30308		**13. Type of Report and Period Covered** Final Report (November 2022–November 2025) **14. Sponsoring Agency Code** N/A
15. Supplementary Notes Conducted in cooperation with the U.S. Department of Transportation, Federal Highway Administration.		

16. Abstract

Bridge scour is a leading cause of hydraulic-related bridge failures, yet current monitoring practices rely on periodic inspections that are insufficient during floods when scour activity accelerates. To address this gap, a low-cost (under $1,000 per unit) remote scour-monitoring system was developed and deployed on two scour critical bridges in Georgia. Each system integrates sonar depth sensors, accelerometers, wireless communication modules, and cloud-based data processing to provide continuous, real-time monitoring.

The system operates in two modes. Under low-flow conditions, vibration data are analyzed with machine learning anomaly detection to establish baseline structural behavior, and under high-flow conditions, models estimate scour depths in conjunction with direct sonar measurements. A custom web interface, Scour View, was developed to visualize data, integrate GDOT's BridgeWatch© alerts, and enable remote control of sensor modes and inspection team allocation during storm events.

Field deployments during three major floods in early 2024 confirmed an inverse relationship between scour depth and bridge vibrational frequency. The system provided accurate, site-specific scour measurements, and comparisons with the Colorado State University (CSU) scour equation highlighted consistent underprediction by the empirical model.

The study demonstrates the feasibility of a scalable, cost-effective scour monitoring platform that enhances bridge safety and resilience during extreme hydrologic events. Future improvements include expanded deployment, integration of velocity and camera sensors, and edge-computing solutions for fully autonomous monitoring.

17. Key Words Scour, Remote Monitoring, Sensor System, Cost-Efficient, Scour View, Machine Learning, Structural Analysis, Optimization	**18. Distribution Statement** No Restrictions		
19. Security Classification (of this report) Unclassified	**20. Security Classification (of this page)** Unclassified	**21. No. of Pages** 109	**22. Price** Free

Form DOT F 1700.7 (8-72) **Reproduction of completed page authorized.**

GDOT Research Project 22-19

Final Report

REMOTE BRIDGE HEALTH MONITORING FOR SCOURING USING COST-EFFICIENT SENSING TECHNOLOGY

By

Tien Yee[1], Ph.D.
Professor

Jidong J. Yang[2], Ph.D., P.E., F.ITE
Associate Professor

Metin Oguzmert[1], Ph.D., P.E., S.E.,
Professor

Mahyar Amirgholy[1], Ph.D.
Associate Professor

Alan Kazemian[1], Ajoy Sarkar[1], Md. Shamsul Alam[1], and Penghao Deng[2]
Graduate Research Assistant

[1] Kennesaw State University
[2] University of Georgia

Contract with
Georgia Department of Transportation

In cooperation with
U.S. Department of Transportation, Federal Highway Administration

November 2025

DISCLAIMER STATEMENT

This document is disseminated under the sponsorship of the Georgia Department of Transportation and the United States Department of Transportation in the interest of information exchange. The State of Georgia and the U.S. Government assume no liability of its contents or use thereof.

The contents of this report reflect the views of the authors, who are responsible for the facts and accuracy of the data presented herein. The contents do not necessarily reflect the official policies of the Georgia Department of Transportation or the U.S. Department of Transportation.

The State of Georgia and the U.S. Government do not endorse products of manufacturers. Trademarks or manufacturers' names appear herein only because they are considered essential to the object of this document.

SI* (MODERN METRIC) CONVERSION FACTORS

APPROXIMATE CONVERSIONS TO SI UNITS

Symbol	When You Know	Multiply By	To Find	Symbol
		LENGTH		
in	inches	25.4	millimeters	mm
ft	feet	0.305	meters	m
yd	yards	0.914	meters	m
mi	miles	1.61	kilometers	km
		AREA		
in^2	square inches	645.2	square millimeters	mm^2
ft^2	square feet	0.093	square meters	m^2
yd^2	square yard	0.836	square meters	m^2
ac	acres	0.405	hectares	ha
mi^2	square miles	2.59	square kilometers	km^2
		VOLUME		
fl oz	fluid ounces	29.57	milliliters	mL
gal	gallons	3.785	liters	L
ft^3	cubic feet	0.028	cubic meters	m^3
yd^3	cubic yards	0.765	cubic meters	m^3
	NOTE: volumes greater than 1000 L shall be shown in m^3			
		MASS		
oz	ounces	28.35	grams	g
lb	pounds	0.454	kilograms	kg
T	short tons (2000 lb)	0.907	megagrams (or "metric ton")	Mg (or "t")
		TEMPERATURE (exact degrees)		
°F	Fahrenheit	5 (F-32)/9 or (F-32)/1.8	Celsius	°C
		ILLUMINATION		
fc	foot-candles	10.76	lux	lx
fl	foot-Lamberts	3.426	candela/m^2	cd/m^2
		FORCE and PRESSURE or STRESS		
lbf	poundforce	4.45	newtons	N
lbf/in^2	poundforce per square inch	6.89	kilopascals	kPa

APPROXIMATE CONVERSIONS FROM SI UNITS

Symbol	When You Know	Multiply By	To Find	Symbol
		LENGTH		
mm	millimeters	0.039	inches	in
m	meters	3.28	feet	ft
m	meters	1.09	yards	yd
km	kilometers	0.621	miles	mi
		AREA		
mm^2	square millimeters	0.0016	square inches	in^2
m^2	square meters	10.764	square feet	ft^2
m^2	square meters	1.195	square yards	yd^2
ha	hectares	2.47	acres	ac
km^2	square kilometers	0.386	square miles	mi^2
		VOLUME		
mL	milliliters	0.034	fluid ounces	fl oz
L	liters	0.264	gallons	gal
m^3	cubic meters	35.314	cubic feet	ft^3
m^3	cubic meters	1.307	cubic yards	yd^3
		MASS		
g	grams	0.035	ounces	oz
kg	kilograms	2.202	pounds	lb
Mg (or "t")	megagrams (or "metric ton")	1.103	short tons (2000 lb)	T
		TEMPERATURE (exact degrees)		
°C	Celsius	1.8C+32	Fahrenheit	°F
		ILLUMINATION		
lx	lux	0.0929	foot-candles	fc
cd/m^2	candela/m^2	0.2919	foot-Lamberts	fl
		FORCE and PRESSURE or STRESS		
N	newtons	0.225	poundforce	lbf
kPa	kilopascals	0.145	poundforce per square inch	lbf/in^2

*SI is the symbol for the International System of Units. Appropriate rounding should be made to comply with Section 4 of ASTM E380.
(Revised March 2003)

TABLE OF CONTENTS

LIST OF FIGURES

LIST OF TABLES

LIST OF ABBREAVATIONS AND SYMBOLS

ADXL345	3-Axis Digital Accelerometer
ADXL335	Analog 3-Axis Accelerometer
AI	Artificial Intelligence
AWS	Amazon Web Services
CAP	Concrete Bent Cap
CSU	Colorado State University
CPU	Central Processing Unit
CTM	Cellular Transmission Module
DOT	Department of Transportation
DS3231	Real-Time Clock Module
ESP32	Espressif 32-bit Microcontroller
ESP-NOW	Espressif Wireless Peer-to-Peer Protocol
FFT	Fast Fourier Transform
FHWA	Federal Highway Administration
GDOT	Georgia Department of Transportation
GPS	Global Positioning System
GPRS	General Packet Radio Service
I²C	Inter-Integrated Circuit
L4×4×½	Steel Angle Section Label
LTE-M	Long Term Evolution for Machines
ML	Machine Learning
MIP	Mixed-Integer Programming
MILP	Mixed-Integer Linear Programming
MoE	Mixture of Experts
MPPT	Maximum Power Point Tracking
MTZ	Miller–Tucker–Zemlin
NBI	National Bridge Inventory

PHP	Hypertext Preprocessor
RTC	Real-Time Clock
RMSE	Root Mean Square Error
SDOF	Single-Degree-of-Freedom
STFT	Short-Time Fourier Transform
SR04T	Sonar Sensor Model JSN-SR04T
SQL	Structured Query Language
TCXO	Temperature-Compensated Crystal Oscillator
TCA9548A	I²C Multiplexer Model
TRIMS	Tennessee Roadway Information Management System
USDOT	United States Department of Transportation
VRPTW-TC	Vehicle Routing Problem with Time Windows and Technician Constraints
Hz	Hertz
m/s	Meter per Second
Ft	Feet
S or Sec	Second
kips/in or k/in	kilo-pounds per inch
B	set of bridges to inspect
T	set of inspection teams
s	Per-bridge inspection time (minutes)
$a_{t,\beta}$	Travel time from team t's base $s(t)$ to bridge b
$r_{t,\beta}$	Return travel time from bridge b back to team t's base $s(t)$
$d_{i,j}$	Bridge-to-bridge travel time from bridge i to j
λ	Weighting factor balancing total working time vs. workload equity.
$x_{t,b}$	Assignment variables, 1 if bridge b is assigned to team t; 0 otherwise
$y_{t,i,j}$	Routing variable, 1 if team t visits j immediately after i; 0 otherwise
u_i	classic Miller–Tucker–Zemlin (MTZ) order variable used to prevent subtours
τ_t	total working time of team t
τ	average team time

$\delta t \geq 0$	absolute deviation of team t's time from the average
x_{ijk}	Binary variable = 1 if vehicle k travels from node i to j
K	Set of available vehicles
N	Set of service nodes
e_i	Lower bound of maintenance
l_i	Upper bound of maintenance
r_i	The number of technicians required at location i
s_i	The maintenance duration at location i
d_{ij}	Real-time travel time from location i to location j

EXECUTIVE SUMMARY

Scouring is a major concern for highway bridges and remains one of the leading causes of bridge failures in the United States. Currently, the Georgia Department of Transportation (GDOT) relies on periodic inspections and post-storm manual measurements to assess scour conditions. Although effective for after-event evaluation, this approach has two key limitations: (1) inspection crews must be deployed immediately following storms, often with limited personnel available, and (2) field conditions may pose safety risks when scour depths are unknown in advance. Commercial scour monitoring systems exist, but they are often costly and lack the flexibility needed for GDOT applications. As such, there is a critical need for a cost-effective and safer solution that enables near real-time monitoring of bridge health during storm events.

This project developed a low-cost, remote scour monitoring system using accelerometers and sonar depth sensors integrated with cloud-based data processing and machine learning (ML). The system collects vibration and scour depth data under both flood and non-flood conditions, transmitting information in real time to a web-based dashboard called Scour View. Scour View not only provides visualization of sensor data and integrates BridgeWatch© alerts, but it allows for optimized inspection team deployment. During field testing, the system demonstrated the ability to distinguish between flood and non-flood conditions, estimate scour depths during high flows, and send automated alerts to GDOT personnel when extreme scour activity was detected.

The system shows strong potential for improving bridge safety and reducing inspector risk; however, several areas for improvement remain. Sensors mounted to bridge bents must withstand harsh environmental conditions, requiring refined mounting strategies for different bridge types.

Deployment on larger bridges may present logistical challenges, and the ML models require additional flood event data to strengthen predictive accuracy. Future work should expand deployment across diverse geographic regions with varying soil conditions, extend monitoring durations to capture more flood events, and integrate additional sensing technologies such as flow velocity and camera systems. These enhancements will improve reliability, broaden applicability, and support GDOT's long-term goal of establishing a resilient, real-time scour monitoring network across the state.

CHAPTER 1. INTRODUCTION

Local scouring is the leading cause of and accounts for approximately 64 percent of bridge failures within the United States (Prendergast and Gavin 2014). The severity of local scouring on bridge piers depends on various factors, such as the shape and size of the bridge piers, hydraulic conditions, and bed sediment sizes. These variables are bridge-specific (pier design) and location-dependent (local flow and soil conditions); therefore, accurate prediction of local scours can be extremely challenging. Because scouring is an unavoidable naturally occurring phenomenon, it is a major concern for highway bridges. Excessive scour on bridge bent or pier, such as that shown in figure 1, may compromise the stability of the structure, and therefore any remediation actions must be conducted in a timely manner. For this reason, scour depths are often measured after severe storm events and used as an important variable to evaluate the health of a bridge.

Figure 1. Photo. Natural loss of sediment from base of bridge bent or pier due to scouring.

Bridges are often inspected for scouring periodically and especially after large storm events to ensure the health and safe operation of bridges. In practice, the Georgia Department of Transportation (GDOT) conducts manual scour depth measurements after storm events to determine the scour extent on bridge piers. Manual measurements are good for assessing post-flood conditions of bridges, but there are major disadvantages to this practice. First, manual measurements require the GDOT inspection crew to be on standby for deployment immediately after a storm event. More often than not, bridge inspectors have very little time to mobilize and monitor bridges at risk of scour (Idaho Water Science Center 2020). Depending on the number of available personnel, GDOT may not be able to perform the inspection for all affected bridges quickly. Second, without prior knowledge of the extent of scour depths during floods, a post-flood inspection may pose a safety concern for the inspection crews.

Countermeasures such as producing hydrodynamic pier designs and armoring pier foundations with riprap are available. However, these techniques are intended for new bridge designs and, additionally, due to hydraulics and other natural uncertainties, the effectiveness of such countermeasures is relatively limited (Sturm et al. 2004). The more economical and effective method to combat scouring is to monitor its evolution over time and implement rehabilitation and repair actions when necessary (Prendergast and Gavin 2014). Thus, there is clearly a need for a remote, cost-efficient system to monitor scours that can be integrated with a decision-making process to help GDOT in mobilizing its inspection teams. This project focuses on building a customized remote bridge monitoring system that can be used to alleviate some of these issues.

CHAPTER 2. LITERATURE REVIEW

A variety of instruments have been traditionally used for monitoring local scours, such as sonar, magnetic sliding collars, float-out devices, tilt sensors, time domain reflectometers (TDRs), and sounding rods (Briaud et al. 2011). These conventional monitoring technologies are not fully efficient in terms of functionality and economy (Mueller 2000), and the advantages and disadvantages of various methods are summarized in table 1.

Table 1. Comparison of monitoring methods of bridge scour.

Instrument	Advantages	Disadvantages	Economic
Magnetic sliding collar	Easy to install and operate; can be used during floods	Cannot collect data continuously; limited region	Good
Float-out device	Easy to install and operate; self-contained	Only provides information when the scour surpasses a critical value; limited region	Excellent
Smart rock	Easy to install and operate; cost-effective; larger region	Limitation on monitoring due to the refill process	Excellent
Sonar	Easy to install; can monitor the refill process; accurate data collecting	Susceptible to the situation of flowing water; difficult toanalyse and interpret	Good
Fiber Bragg grating sensor	Continuous monitoring	Time-consuming; special training required; destroyed easily	Poor
TDR	Easy to install and operate; can monitor the refill process; real-time monitoring	Limited monitoring region for each sensor; excavation required	Good
Tilt sensor	Easy to analyze and interpret	Influenced by traffic, temperature, wind, and hydraulic factors	Excellent
Modal parameter	Environment friendly; easy to operate	Special training required; influenced by traffic, piers, and hydraulic factors	Excellent

Among the instruments listed in table 1, only a few options are identified as economical: the float-out device, smart rock, tilt sensor, and modal parameter. Mueller's study also mentioned that the modal parameter method is still in its early development stage with no direct field validation of its sensitivity and reliability, and therefore its practical application in the field is limited. It should be noted that many of the instruments are used as tools for data collection and do not necessarily provide direct feedback on field conditions. Not until recently have cost-efficient sensors been available, and thus low-cost systems have become viable for modal parameter monitoring (Komarizadehasl et al. 2021). As indicated in the literature, although technology is still in its infancy, it has been conceptually proven to be capable of collecting data for monitoring purposes.

Common practices of the state departments of transportation (DOTs) in monitoring scours have been reviewed. GDOT is currently using a proprietary software program called BridgeWatch© to monitor critical bridges (Scannell and Baribault 2010), which requires field inspection immediately following a flood event. Tennessee, Michigan, Pennsylvania, New York State, and Idaho DOTs use very similar approaches in scour monitoring (Curtis et al. 2017). Only a few states (i.e., Minnesota, Missouri, and California) use more sophisticated instruments to monitor scours. These common practices of scour monitoring from various DOTs are summarized in table 2.

Table 2. Common practices used by state DOTs to monitor scours.

State DOT	Practices/Tools Used
Tennessee	Software monitoring – BridgeWatch, Tennessee Roadway Information Management System (TRIMS), FB-MultiPier
Iowa	Hydrographic survey using echo sounder
Texas	Interference and geophysical method
Pennsylvania	Rainfall forecaster, National Oceanic and Atmospheric Administration (NOAA), AccuWeather alert
Florida	Risk-based calculations
Mississippi	Instrumentation and inspection
Minnesota	Fixed sonar, float-out device, tethered switches
Michigan	MiBRIDGE – web-based bridge management and field inspection module
Colorado	Instrumentation and inspection
New York State	Screening and monitoring (did not mention instrumentation)
Missouri	U.S. Geological Survey (USGS) real-time riverbed monitoring, smart rock scour monitoring, bathymetric and velocimetry survey light detection and radar (LiDAR) scan
Idaho	BridgeWatch
California	Sonar, 2D and 3D modeling, inertia navigation system, tilt sensor, sliding magnetic collar, smart rock, acoustic stage gauge

The summary provided in table 2 shows that software such as BridgeWatch© is one of the tools used for monitoring. BridgeWatch© does not provide information on scour but, rather, is an alert system to notify DOTs of potential bridges that may experience concerning flow conditions and thus warrant the deployment of crews for field inspection.

Many of the instrumentations mentioned in table 2 are designed and used only for the sole purpose of scour observations, and because scouring may compromise structural integrity, it is also equally important to monitor a bridge's health alongside scour evolution. In 2011, the

laboratory study by Briaud et al. (2011) showed that scours could alter the vibration behavior of a bridge pier, characterized by a sharp decrease in its natural frequencies when the scour depth reaches the bottom of the bridge footing, as indicated in figure 2 at the 4.5-h mark of the test.

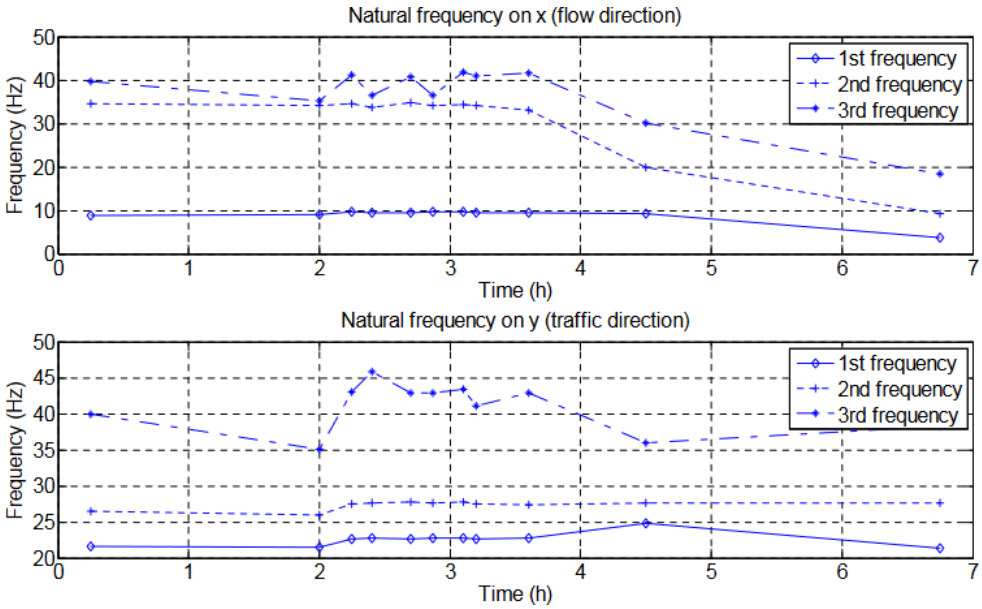

Figure 2. Graphs. Laboratory test on influence of scour on piers (Briaud et al. 2011).

Figure 2 reveals two important characteristics of bridge vibration behaviors prior to severe scouring. First, the vibration frequencies decrease significantly for all modes of frequencies when scour reaches the bottom (past 4.5 h) of the pier column. Second, the steepest descending gradient in the first and second natural frequencies happens before the scour reaches the bottom of the pier. These two characteristics indicate that the vibration on bridges must have deviated from normal just before or after the scour reaches the bottom of the pier footing.

CHAPTER 3. PROPOSED SYSTEM ARCHITECTURE

In this project, the research team proposes to capture such anomaly behaviors using modern machine learning (ML) techniques that harness real-time sensor data. Along with monitoring scour depths, monitoring the vibration behavior of bridge piers helps to capture and provide early warning of potentially dangerous events. An ideal system can provide remote monitoring capability and receive continuous data feeds on hydraulics and/or scouring data as well as structural properties of the bridges, especially at critical times, such as during and immediately after flooding events. Continuous scour and health monitoring provides the convenience of examining bridge health and making crucial and time-sensitive closure, maintenance, or rehabilitation decisions. The existing commercial bridge health monitoring system is limited in functionality and lacks power in behavior modeling and prediction. As such, there is a clear need for a scour and bridge health monitoring system that can work in unison with the existing GDOT scour monitoring system and protocols. Coupled with the BridgeWatch© software currently employed by GDOT, the proposed monitoring system provides essential local data to aid decision-making for short- and long-term bridge closures, maintenance, and repairs, and also the optimal allocation of resources and deployment of the inspection teams.

The primary goals of this project are to (1) develop a remote health monitoring system for highway bridges in Georgia using cost-efficient sensing technology, (2) integrate modern ML techniques to help monitor and warn of any vibrations and behavioral anomalies, and (3) optimize the response and maintenance operation based on the data collected from the sensors. These goals will be further discussed in the following chapters.

To achieve these goals, the research team will make use of low-cost depth sensors and accelerometers to estimate scour depths, vibration, and tilt of bridge piers. The data collected from the sensors will be analyzed using an ML approach to warn the bridge and maintenance engineers of any sensed anomaly. In addition, an optimization algorithm will be developed to assist GDOT in the decision-making process for human resource allocation immediately after a large storm event.

At the high level, the remote scour monitoring system consists of three major subsystems, namely, the physical sensors and communication unit, the cloud computing platform, and the local server or computer. The three parts will communicate with each other and function as a system as shown in figure 3.

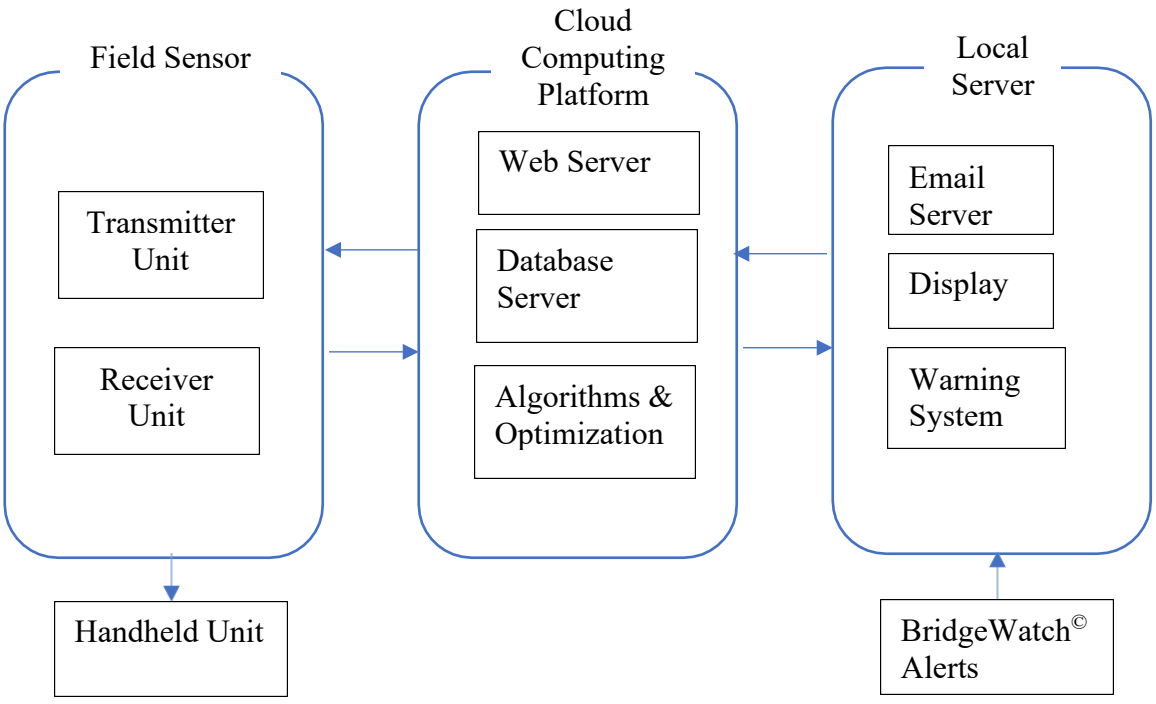

Figure 3. Flowchart. High-level architecture of the remote scour monitoring system.

The field sensor subsystem consists of two parts: the transmitter unit and the receiver unit. The function of the transmitter unit is purely to collect data (i.e., depths, accelerations, and time) at the bridge pier or bent; thus, this unit will be attached to the pier or bent being monitored. The transmitter will collect the necessary data and send it to the receiver unit. The receiver unit accepts the data from the transmitter unit and stores and sends the data to the cloud environment. The field sensor unit is also where the majority of the hardware will be needed. For further clarity, the circuitry of the field unit, specifically the transmitter unit is shown in **Figure 4**below.

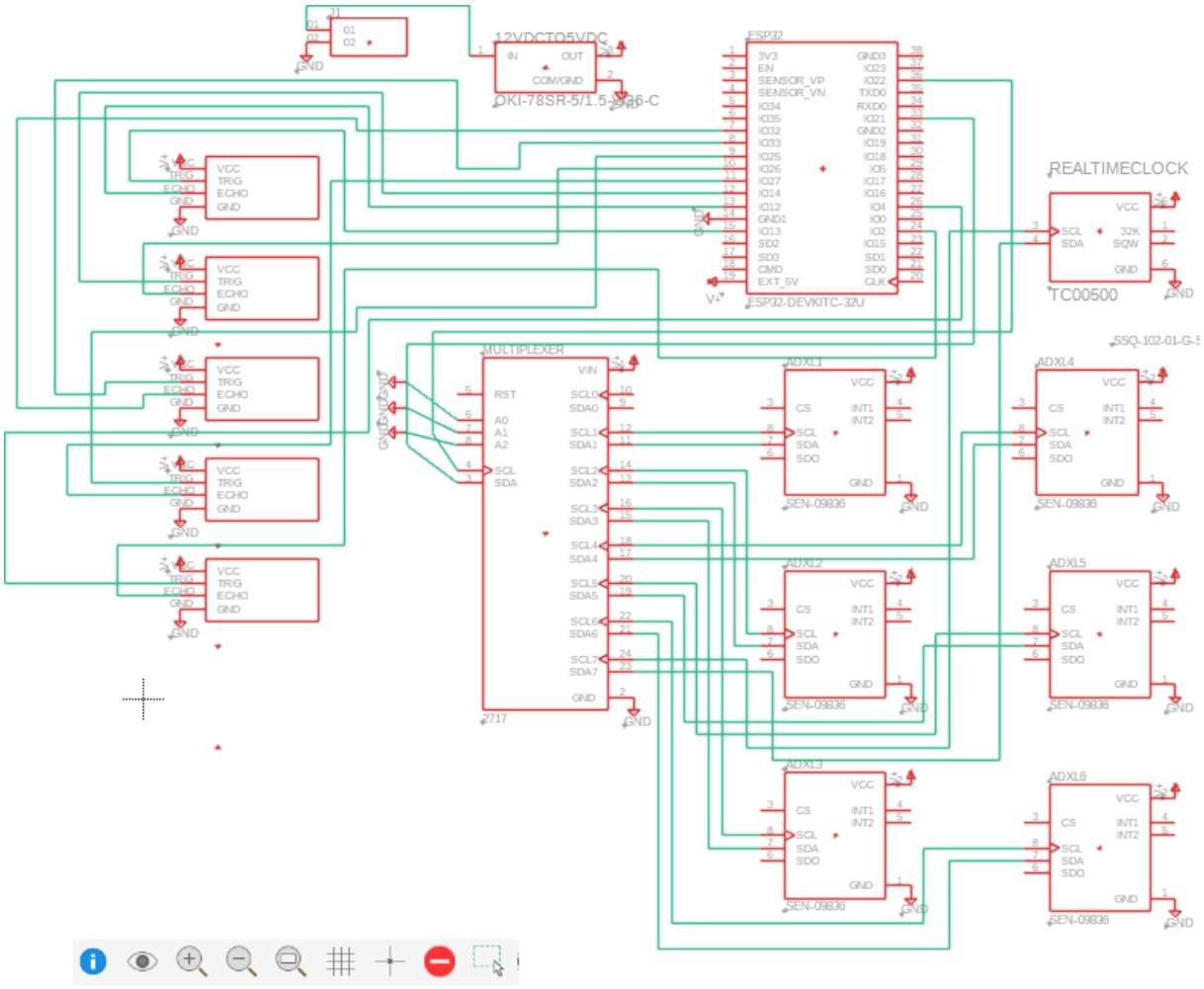

Figure 4. Diagram. Circuit diagram for a typical transmitter unit.

The second subsystem, which consists of the cloud computing platform, is where most of the heavy computing will occur. The web server, database server, and algorithms will be housed under this subsystem. The web server is the “host” that will receive the communication from the receiver unit. Once the data are received, the web server then parses the data onto the database for storage. The data will then be pulled from the database for display purposes and for use by the other algorithms and optimization codes. The algorithms and optimization codes include the ML codes necessary for the system, the team assignment optimization codes, and the warning trigger for the alert system.

After data are stored and processed, the third subsystem is the user-end subsystem. It may be a local server or as simple as a personal computer. The local computer will be where the data are displayed, emails are received, and possibly where a simple email server will reside. This is also where users can remotely control the functionality of the field sensors and monitor scour data, activities, and warnings.

CHAPTER 4. HARDWARE COMPONENTS

COMPONENT SELECTION

The components for the vibration-based scour detection system were chosen following a rigorous selection process aimed at ensuring optimal performance, reliability, and compatibility with the overall system requirements. This first initial critical phase involved an evaluation of various factors, including but not limited to technical specifications, functional capabilities, cost-effectiveness, and vendor reputation.

ACCELEROMETERS

To ensure alignment with the project's objectives, anticipated outcomes, and technical requirements, extensive research was conducted on potential system components. This process involved reviewing industry standards, technical literature, and supplier catalogs to compile a comprehensive set of viable options. Among the first tasks was the identification of accelerometers capable of detecting vibrations with high sensitivity while operating effectively near the direct current (DC) frequency range (0 Hz). Cost considerations were also incorporated into the evaluation. The selected accelerometers reflect both established field practices in vibration monitoring and recommendations supported by the literature. A comparative analysis of accelerometers with different sensitivities and price points that are commonly applied in civil structures worldwide is presented in table 3**.**

Table 3. Accelerometer comparison table.

Name	Price	Acceleration Range (g)	Frequency Range	Spectral Noise	Operation Temperature	Structural Type	Type
3713B112G	2070.0	+2.0	[0.00, 250]	22.90	[−54, +121]	Wind Turbine	Tri, M
356B08	1610.0	+50.0	[0.50, 5000]	40.00	[−54, +77]	Bridge Crane	Tri, P
356A45	1410.0	+50.0	[0.70, 7000]	125.00	[−54, +85]	Forward Swept Wing Motorbike	Tri, P
356B18	1300.0	+5.0	[0.50, 3000]	11.40	[−30, +77]	Speedway Stadium	Tri, P
3711B1110G	870.0	+10.0	[0.00, 1000]	107.90	[−54, +121]	Railroad Bridges	Uni, M
KS48C	750.0	+6.0	[0.25, 130]	0.60	[−20, +120]	Footway Bridge Historical	Uni, P
393B12	820.0	+0.5	[0.15, 1000]	1.30	[−54, +82]	Masonry Structures	Uni, P
352C33	380.0	+50.0	[0.50, 10,000]	39.00	[−54, +93]	Bridges	Uni, P
ADXL335	10.7	+3.6	[0.50, 550]	300.00	(−40, +85)	Bridges	Tri, M
LIS344ALH	12.0	+2.0	[1.00, 500]	50.00	[−40, +85]	Steel beam	Tri, M
MPU9250	5.8	+16.0	[0.24, 500]	300.00	[−40, +85]	Steel Pile and Column	Tri, M
MPU6050	5.4	+16.0	[0.24, 500]	400.00	[−40, +85]	Building Model	Tri, M

Note: Adapted from Komarizadehasl et al. (2021).

After evaluating multiple accelerometers based on cost, frequency response, axis configuration, and size, the ADXL345 was selected as the most suitable option. Compared to its predecessor, the ADXL335, the ADXL345 provides an extended frequency range, higher resolution, and triaxial capability, while maintaining a comparable price point. Its balance of performance, affordability, and compact size makes it the optimal choice for this project. The selected accelerometer is shown in figure 5.

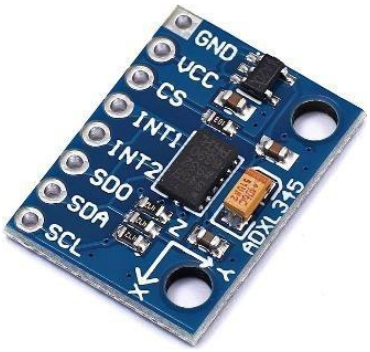

Figure 5. Photo. ADXL345 accelerometer.

During the review of the literature, the concept of combining multiple accelerometers into a single system emerged as a cost-effective alternative to using high-priced individual units. After evaluating various configurations, six accelerometers were selected to operate together, providing greater sensitivity than a single triaxial accelerometer costing several thousand dollars. By synchronizing their data, the system achieves improved vibration detection at a fraction of the cost. This approach also offers scalability, as additional accelerometers can be integrated if future expansion is required. Ultimately, the decision balanced cost, size, and performance, resulting in a low-cost yet highly effective solution for advanced vibration monitoring.

SONAR SENSORS

Following the selection of accelerometers, the JSN-SR04T sonar sensor was chosen for its accuracy, cost-effectiveness, and ease of integration with microcontroller platforms such as the ESP32 and Arduino. With a detection range of up to 15 ft and reliable performance, it met the project's requirements for distance monitoring.

A key advantage of the JSN-SR04T is its potential for underwater operation, allowing the system to function both above and below the water's surface—an essential feature for this application. Five units were deployed and tested across air, surface, and underwater environments, with

validation results presented in CHAPTER 5CHAPTER 5. Figure 6 shows the JSN-SR04T sonar transmitter and receiver used in the system.

Figure 6. Photo. JSN-SR04T sonar transmitter and receiver.

By complementing the accelerometers with precise distance measurement, the JSN-SR04T enhances the system's overall monitoring capability.

MICROCONTROLLER (TRANSMITTER)

Alongside the selection of sensors, a central control unit was required to coordinate all components and manage data processing. Following a thorough evaluation, the ESP32 microcontroller was selected as the most suitable option. Its strong processing capabilities, combined with built-in Wi-Fi and Bluetooth, enable efficient communication and control across system components. The chosen ESP32 module also includes an on-board antenna port, allowing connection of an external antenna to extend communication range between modules (see figure 7).

Figure 7. Photo. ESP32 microcontroller with on-board antenna.

In comparison to Arduino boards, the ESP32 was favored for its support of ESP-NOW, a protocol that enables direct, seamless data transmission between ESP32 modules. This feature significantly improves efficiency and reliability in system communication (see figure 8).

Figure 8. Diagram. ESP32 ESP-NOW communication.

The ESP32's wireless functionality ensures effective synchronization between the accelerometers, sonar sensors, and other peripherals, providing a scalable and adaptable platform

for system development. The integration of the ADXL345 accelerometers, JSN-SR04T sonar sensors, and ESP32 microcontroller represents a key milestone in advancing the vibration monitoring system, enabling robust performance across diverse environmental conditions.

MULTIPLEXERS

To manage communication from the growing number of sensors, the TCA9548A I²C multiplexer was integrated into the system. This device supports up to eight independent I²C buses, allowing the ESP32 to assign unique addresses to each sensor and handle multiple data streams efficiently.

By isolating sensors on separate buses, the multiplexer minimizes crosstalk, improves data integrity, and ensures stable communication in complex environments. Its low power consumption further enhances system efficiency. As shown in figure 9, the TCA9548A provides a reliable and scalable solution for managing the expanding sensor array.

Figure 9. Photo. TCA9548A multiplexer.

REAL-TIME CLOCK AND TEMPERATURE SENSORS

To ensure accurate timekeeping for data synchronization, the DS3231 real-time clock (RTC) module was integrated into the system. The DS3231 was selected for its exceptional accuracy (within a few seconds per year), its low power consumption, and the stability provided by its

temperature-compensated crystal oscillator (TCXO). Its built-in temperature sensor further enhances reliability in fluctuating environments.

With a simple I²C interface, the DS3231 integrates seamlessly with the multiplexer and ESP32 microcontroller, reducing development effort. As shown in figure 10, the DS3231 provides precise, energy-efficient, and stable timekeeping, ensuring reliable synchronization and analysis for the monitoring system.

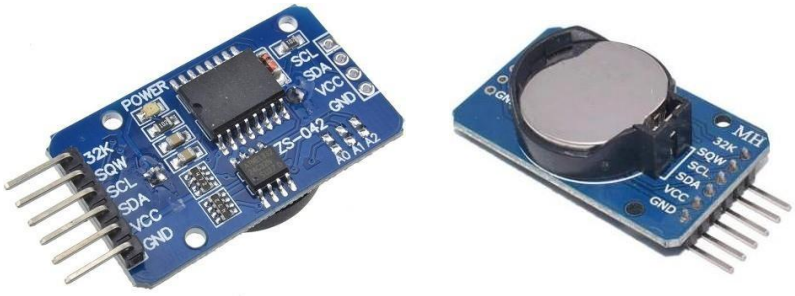

Figure 10. Photo. DS3231 RTC with temperature sensor.

MICROCONTROLLER (RECEIVER)

To enable reliable data transmission for monitoring and analysis, the SIM7000 ESP32 module was integrated into the system. This module provides seamless compatibility with the ESP32 microcontroller, supports local data storage, and offers cellular connectivity (i.e., GSM, GPRS, or LTE), ensuring operation even where Wi-Fi or Ethernet is unavailable.

For added reliability, two SIM7000 modules were deployed: one dedicated to transmission and the other as a backup for local storage. This redundancy safeguards data during connectivity interruptions, ensuring continuous and secure collection. As shown in figure 11, the SIM7000 receiver module enhances the system's resilience by delivering stable and adaptable wireless communication.

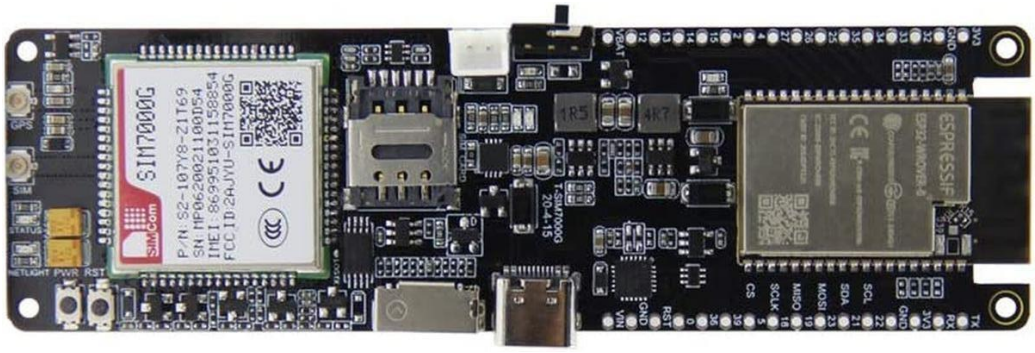

Figure 11. Photo. SIM7000 receiver module.

ASSEMBLED TRANSMITTER AND RECEIVER UNITS

The individual components were placed into the transmitter box and receiver box to form their subsystems. The receiver and transmitter units were then fitted into enclosures that were weatherproofed to handle the field environment, as shown in figure 12 and figure 13, respectively.

Figure 12. Photos. Receiver assembly and enclosure.

Figure 13. Photos. Transmitter assembly and enclosure.

The two units worked together to form the on-site main data collection hardware for this project. Depending on the relative location of the receiver unit to the transmitter unit, a solar panel was also added to charge the battery and power both the transmitter and receiver units during the daytime. The battery was also sized to last for a minimum of 7 days without charging.

APPROXIMATE COST OF SYSTEM (HARDWARE)

A unit of the system costs approximately $895.00. The breakdown of the cost for the hardware is shown in table 4.

Table 4. Approximate hardware cost for the system.

Components	Quantity	Unit Cost	Subtotal
Mounting hardware	1	$100.00	$100.00
Accelerometers	6	$4.00	$24.00
Depth sensor	5	$8.00	$40.00
Multiplexer	1	$13.00	$13.00
ESP32	1	$25.00	$25.00
ESP32 with SIM7000	1	$70.00	$70.00
RTC	1	$5.00	$5.00
Cellular antenna	1	$33.00	$33.00
12V gel battery	1	$80.00	$80.00
MPPT[1] charge controller	1	$50.00	$50.00
USB cable	1	$10.00	$10.00
Wires	1	$20.00	$20.00
Receiver enclosure	1	$90.00	$90.00
Transmitter enclosure	1	$50.00	$50.00
Solar panel	1	$50.00	$50.00
Solar panel pole mount kit	1	$50.00	$50.00
Receiver pole mount kit	1	$20.00	$20.00
Flexible conduit	1	$25.00	$25.00
SIM card	1	$10.00	$10.00
SD card	2	$15.00	$30.00
Customized circuit board	1	$100.00	$100.00
		Total	**$895.00**

[1] MPPT = Maximum Power Point Tracker

CHAPTER 5. CALIBRATION, VALIDATION, AND HARDWARE–SOFTWARE COUPLING

Prior to deployment, the sensor units were calibrated and validated to ensure reliable operation in the field. This process began with individual component testing, followed by system-level integration and verification. To ensure consistent performance, careful attention was given to sensor sensitivity, environmental conditions, and data acquisition.

ACCELEROMETER CALIBRATION

The first step involved calibrating and validating the six ADXL345 accelerometers (described in Accelerometers). These sensors play a critical role in detecting vibrations associated with potential scouring. To ensure accurate readings, each accelerometer was individually adjusted for sensitivity variations arising from manufacturing differences and environmental conditions at rest.

Calibration was performed using the Shake Table II by Quanser (see figure 14), a testing apparatus capable of generating controlled vibrations across a frequency range of 0–3 Hz.

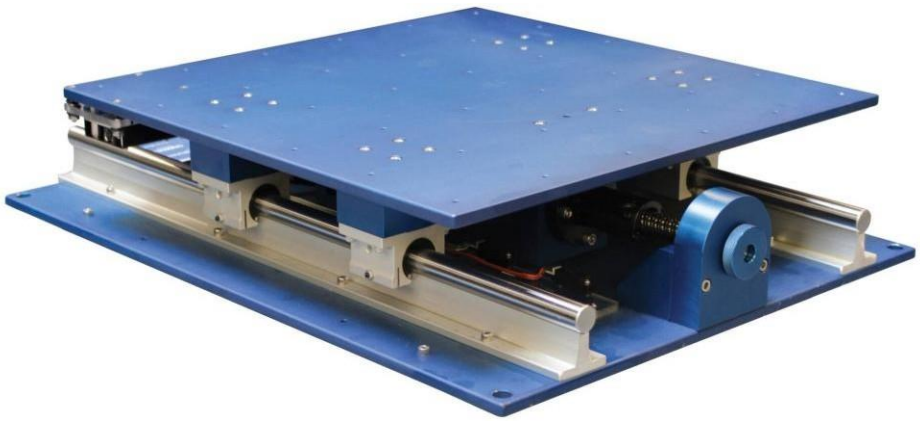

Figure 14. Photo. Quanser Shake Table II.

The accelerometers were exposed to vibration patterns of varying frequencies and amplitudes using Quanser software, generating a comprehensive dataset to characterize sensor response under operational conditions.

Recorded outputs were compared against theoretical models and calibration standards, providing the basis for sensitivity adjustments. Table 5 presents the results of these tests, confirming that the accelerometers accurately captured vibration frequencies. In addition to frequency validation, sensor positioning was optimized on the board to minimize measurement errors. Averaging across the calibrated accelerometers was employed to reduce fluctuations and noise in output data. The calibration goal was to ensure that stationary accelerometers recorded values close to 0, 0, and 9.81 m/s^2 along the x-, y-, and z-axes respectively, thereby enabling accurate detection of vibration changes associated with scouring events.

Table 5. Output of Shake Table II amplitudes and frequencies based on vibration-based device.

Shake Table Amplitude	Shake Table Frequency	FFT* Amplitude	FFT* Frequency	Scaling Factor	Visualization
1	0.25	0.9830	0.2526	0.00046	Difficult to See
1	0.50			19.00	Easy to See
1	1.00	1.0250	1.0160	8.00	Very Easy to See
1	2.00	0.9665	2.0146	1.70	Very Easy to See
1	3.00	0.9885	3.0124	0.61	Very Easy to See
0.500	0.25	0.4888	0.2489	55.00	Difficult to See
0.500	0.50	0.4984	0.4927	18.00	Easy to See
0.500	1.00	0.4991	1.0110	5.40	Very Easy to See
0.500	2.00	0.4915	2.0031	1.25	Very Easy to See
0.250	0.25	0.2458	0.2439	72.00	Difficult to See
0.250	0.50	0.2518	0.4978	17.00	Easy to See
0.250	1.00	0.2483	0.9922	4.80	Very Easy to See
0.250	2.00	0.2516	2.0094	1.50	Very Easy to See
0.250	3.00	0.2547	3.0182	0.70	Very Easy to See
0.100	0.25	0.0954	0.2585	80.00	Difficult to See
0.100	0.50	0.0995	0.5134	24.00	Easy to See
0.100	1.00	0.0911	1.0040	5.00	Very Easy to See
0.100	2.00	0.0949	2.0059	1.30	Very Easy to See

* FFT = Fast Fourier Transform

SONAR SENSOR CALIBRATION

Following the accelerometer validation, calibration efforts focused on the JSN-SR04T sonar depth sensors (described in Sonar Sensors) for both above- and below-water use. Preliminary tests assessed operational limits by suspending sensors at various heights. Results indicated a reliable measurement range of approximately 0.8–1.0 ft minimum and 15 ft maximum. These findings established thresholds for detecting rising water levels and allowed proper calibration of the control code.

The sonar's 60° field of view was evaluated to determine coverage and obstacle interference (see figure 15). This wide-angle capability allowed comprehensive water depth monitoring and informed installation strategies to reduce false readings.

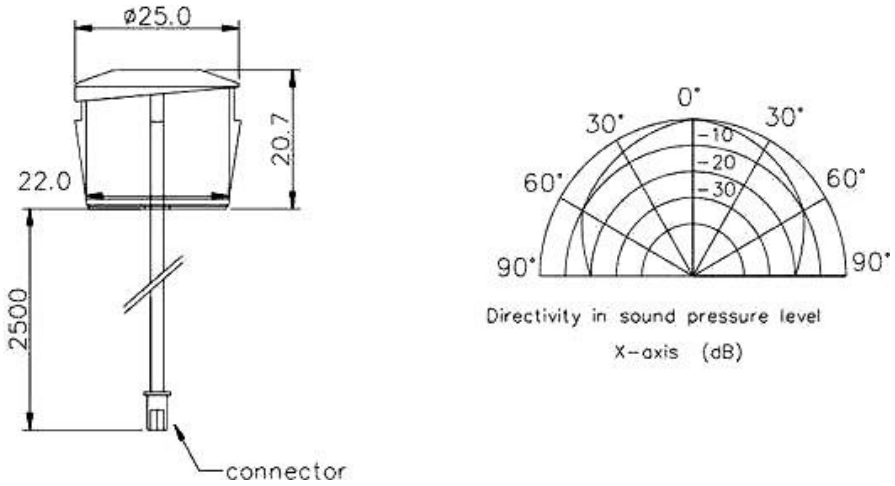

Figure 15. Diagram. JSN-SR04T sonar sensor dimensions and directivity.

For underwater testing, additional calibration was required due to the distinct acoustic properties of water. At 20°C, sound travels at 343 m/s in air versus 1,481 m/s in water, moving approximately 4.3 times faster underwater. As such, sensor parameters such as pulse duration and beam width were fine-tuned for subaqueous operation. Controlled tests in varying depths (see figure 16 and figure 17) confirmed reliable performance, ensuring accurate detection of water depth and scouring activity across both environments.

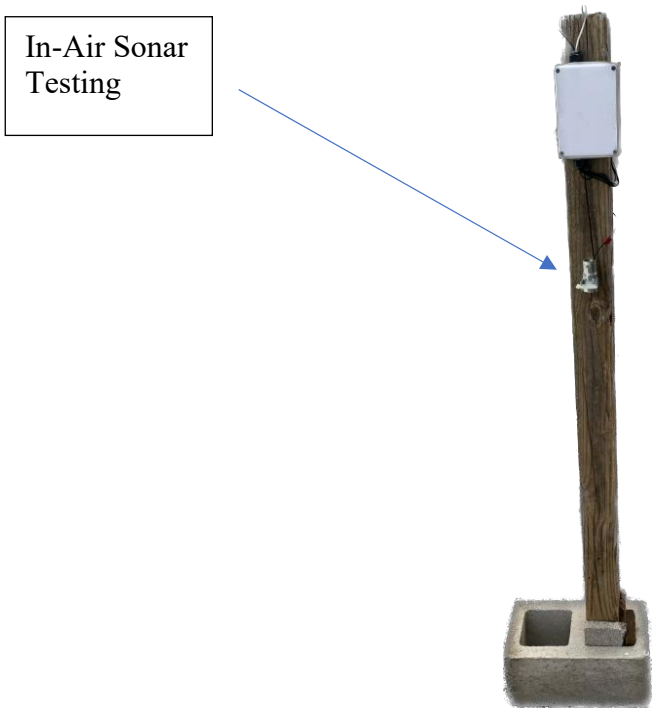

Figure 16. Photo. Mock pier in-air probe testing.

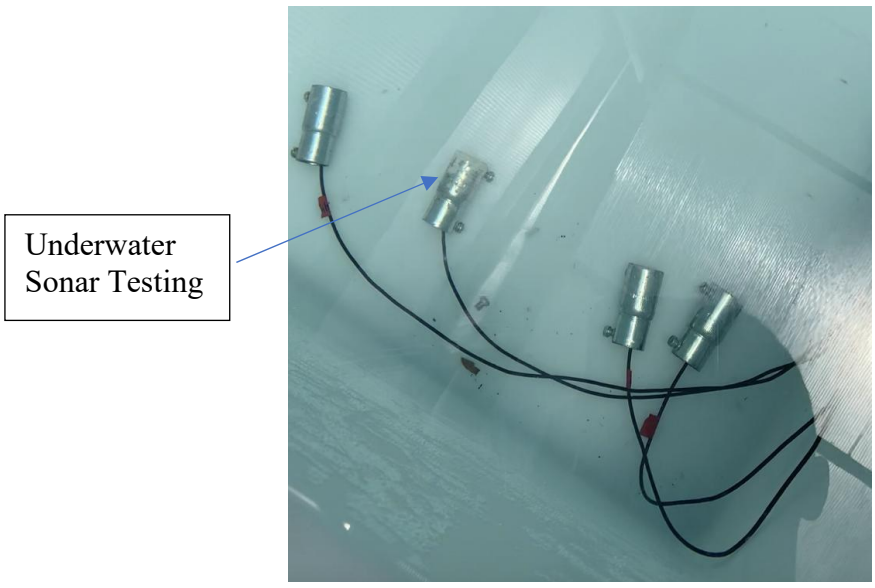

Figure 17. Photo. Underwater sonar system testing.

HARDWARE AND SOFTWARE COUPLING

With all components calibrated, attention shifted to hardware–software integration. The transmitter and receiver units were assembled and tested using a local server.

Transmitter Unit

The transmitter was first validated under normal operating mode, where data are collected at 5-min intervals. It was then tested in rapid collection mode (Rapid Fire Mode), capturing accelerometer readings every 0.013 s. The latter mode is designed for flood conditions, where rapid data collection is critical to capture dynamic bridge responses.

Receiver Unit

The receiver unit, communicating with the transmitter via ESP-NOW, was validated for accurate and lossless data transfer. It incorporates two SIM7000G modules operating in parallel to ensure reliable wireless reception and local storage of transmitted data. A solar panel with MPPT charge controller provides continuous power, maintaining optimal battery levels even under low sunlight or adverse weather conditions.

System power loading was calculated based on current draw, operational duration, and component requirements. This analysis guided proper sizing of the 12V wiring and battery capacity (ampere-hours), ensuring uninterrupted operation during storm events and low-light conditions.

DATA ACQUISITION PROCESS

At each cycle, the system records data from five depth sensors (four underwater and one above water), triaxial accelerometers, an RTC, and temperature sensors. Measurements occur every 5 min (customizable), after which rapid vibration sampling is performed for 5 s and transmitted to the receiver.

The receiver, equipped with dual microcontrollers, parses and stores incoming data locally while formatting packets for transfer to the cloud-hosted database server.

Server-Side System

A MySQL database with phpMyAdmin interface was developed to manage incoming data. MySQL's scalability and reliability made it suitable for continuous monitoring, and phpMyAdmin provided a graphical interface for administration.

The implementation of the server-side system followed these key steps:

- Database Design: Defined schemas, data types, and relationships to optimize storage and retrieval.
- Data Management: Enforced validation rules, integrity constraints, and normalization.
- Server Configuration: Installed MySQL and phpMyAdmin with secure access controls.
- System Integration: Established application programming interfaces (APIs) and scripts to facilitate real-time data transfer from the receiver to the database.
- Monitoring and Maintenance: Implemented backup procedures, performance monitoring, and software patching.

Bidirectional Communication and Operational Modes

An echo-response mechanism was implemented within the PHP scripts, enabling feedback from the database to the receiver and transmitter. Depending on the response value ("0" or "1"), the transmitter transitions between four operational modes:

1. **No Flood Conditions (Troubleshooting Mode):** Samples all sensors every 10 min for baseline monitoring.

2. **Normal Operating Mode (No Flood + Sampling):** Collects data every 5 min, followed by 30 s of rapid vibration sampling.
3. **Flood Awareness Mode:** Monitors water depth sensors; three consecutive incremental increases trigger escalation.
4. **Rapid-Fire Mode:** Collects accelerometer and timing data at maximum speed, while logging full sensor readings once per minute. The system automatically reverts to baseline mode after conditions normalize.

Through rigorous calibration, validation, and integration, the vibration-based scour detection system was optimized for field deployment. Accelerometers were fine-tuned using controlled vibration tests; sonar sensors were validated for both air and water environments; and all hardware was coupled through the ESP32, SIM7000 modules, and efficient power management. The cloud-based MySQL/phpMyAdmin database provided reliable data storage and enabled bidirectional communication for adaptive operational modes. Together, these elements ensured a robust, scalable, and resilient monitoring system capable of delivering accurate real-time insights into bridge scour conditions.

CHAPTER 6. FIELD TESTING AND STRUCTURAL ANALYSIS

The remote monitoring system was installed and tested in the field on two bridges (Bridge 1 and Bridge 2). Both bridges are located in Carroll County on State Route 166, and they were chosen due to the severity of the scours at bents within the waterways. Details of the bridges and their condition are provided in figure 18.

Bridge 1
Bridge ID: 045-0045-0
Crossing: SR 166 over Little Tallapoosa River
County: Carroll County
District: 6
Area: 9
Coordinates: 33.561381974095696, −85.14799599509368
Scour status: 3: Bridge is scour critical; bridge foundations determined to be unstable for calculated scour conditions: (1) Scour within limits of footing or piles; (2) scour below spread-footing base or pile tips.

Bridge 2
Bridge ID: 045-0043-0
Crossing: SR 166 over Big Indian Creek
County: Carroll County
District: 6
Area: 9
Coordinates: 33.54642828984494, −85.28536499652748
Scour status: 3: Bridge is scour critical; bridge foundations determined to be unstable for calculated scour conditions: (1) Scour within limits of footing or piles; (2) scour below spread-footing base or pile tips.

Figure 18. Photos. Details of the two selected Carroll County bridges.

These bridges are also documented as scour critical in the National Bridge Inventory (NBI) report and thus are good candidates for remote health monitoring. For reference, the locations of these bridges are provided in figure 19.

Figure 19. Map. Locations of selected scour critical bridges.

The structural analysis will be presented for Bridge 1 (045-0045-0) for simplicity and brevity.

BRIDGE DESCRIPTION AND SUBSTRUCTURE DETAILS

Bridge 1 in this study is a 1971 cast-in-place concrete T-beam bridge located in northwest Georgia. It carries a two-lane roadway (one lane in each direction) and has an overall length of 400 ft with a deck width of 48 ft. The superstructure consists of concrete T-beams monolithic with the deck, supported by 9 reinforced concrete bents spaced at 40-ft intervals (typical span length). Each bent comprises a cap beam and 6 steel H-piles; the piles are spaced at 9 ft 6 in and driven to an average embedment depth of 18 ft. The reinforced concrete bent cap measures 30 × 28 in. for the cross-section and spans 56 ft along the longitudinal direction of the bridge. The bridge has a skew angle of 25° between the deck and the bent caps. Load transfer from the superstructure to each bent is achieved via plain neoprene elastomeric bearing pads placed between the T-beam girders and the bent cap.

Two of the interior bents (those in the midspan region of the bridge) are permanently submerged in the water and have been classified as scour critical by the local authorities. In other words, these supports are susceptible to scour around their foundations. To improve their lateral stability, the submerged bents are laterally braced with steel angle cross-bracing (L4 × 4 × ½ angles configured in an X-brace between piles). This bracing provides additional lateral stiffness to the bent, which is particularly important for resisting transverse loads and mitigating the effects of potential scour around the pile group.

FIELD VIBRATION TESTING AND IN SITU LATERAL STIFFNESS ESTIMATION

The proposed scour monitoring system was installed on the cap beam of one of the midspan scour critical bents. To characterize the in situ dynamic behavior of this bent (as it currently stands, with existing scour conditions) and to support the calibration of an analytical model for an artificial intelligence (AI)-based scour detection module, an ambient vibration test was conducted. The test aimed to identify the bent's fundamental natural frequency and infer its lateral stiffness under current conditions.

The dynamic testing focused on the bridge's transverse direction that is, the direction parallel to the bent cap (nearly aligned with the river's flow beneath the bridge). This transverse direction was selected because it is less influenced by the superstructure's stiffness and thus is more sensitive to changes in substructure (i.e., foundation) stiffness due to scour. In essence, vibrations measured in the transverse direction are dominated by the response of the bent itself. This makes it easier to detect stiffness changes in the bent caused by scour because the superstructure contributes relatively less restraint in this direction.

Data collection was performed under ambient conditions and light vehicular loading. No heavy external excitation equipment was used; instead, a pickup truck of approximately 4,500 lb served as the dynamic load. The truck was positioned on the bridge deck directly above the instrumented bent (centered at the expansion joint over that support). To generate a lateral vibration, the truck executed a rapid start-and-stop maneuver: it accelerated briefly and then braked hard to a stop over the bend within about a 3-s interval. This sudden braking induced a lateral impulse on the bridge. The maneuver was repeated three times in separate test runs to ensure repeatability, with short pauses between runs to reposition the vehicle and to verify that the data were recorded correctly each time. The braking action is estimated to have applied a lateral force pulse of roughly 700 lb over the 3-s stopping duration. This level of excitation, while relatively small, was sufficient to induce measurable vibrations in the bent and the portion of the bridge it supports.

During each test run, acceleration responses were recorded by accelerometer sensors mounted on the bent cap. The vibration data from the tests were segmented into 10-s time windows for analysis. A Fast Fourier Transform (FFT) was applied to each segment to transform the time domain data into the frequency domain. From the resulting frequency spectra, a dominant frequency peak was consistently observed at 2.68 Hz, corresponding to a vibration period of 0.38 s. This 2.68 Hz frequency is identified as the fundamental natural frequency of the bent (in the transverse direction) under the bridge's current conditions. Sample acceleration time history traces and its FFT spectra from the field test are presented in figure 20. These results establish a baseline dynamic signature of the bent, against which changes (e.g., due to scour) can be later compared.

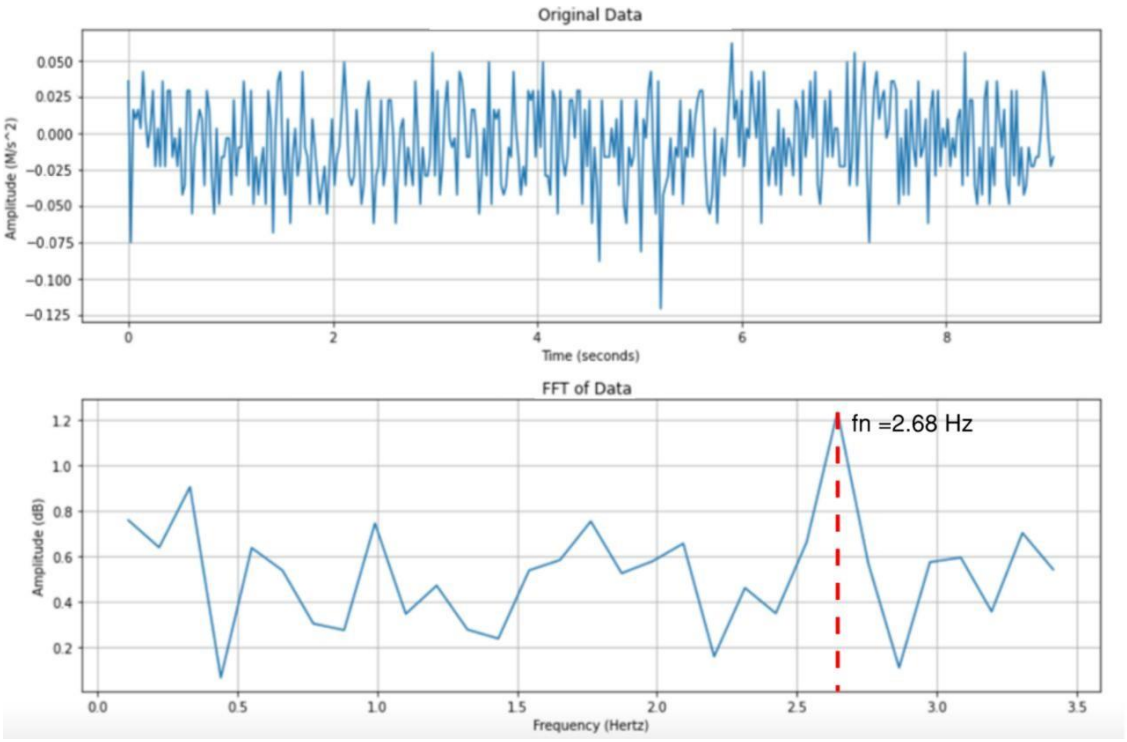

Figure 20. Graphs. Acceleration and FTT data, Brake Test 1.

ANALYTICAL MODELING AND LATERAL STIFFNESS CALIBRATION

To estimate the lateral stiffness of the bent in its current condition (corresponding to the 2.68 Hz frequency observed), a structural model of the bent was developed using SAP2000 (Computers and Structures, Inc. 2023). The model geometry was developed based on as-built drawings and field-verified dimensions of the bent cap and piles. All piles were modeled, with the two outer piles assigned a 1:8 batter as indicated in the as-built drawings and confirmed during field inspection. The average exposed pile length, measured in the field from the riverbed to the cap, was approximately 17 ft 10 in. Given that each pile has roughly 18 ft of additional embedment into the soil below the riverbed, the base of each pile in the model was idealized as a fixed support in both translation and rotation because the soil below that depth provides substantial restraint. The steel angle cross braces (L4 × 4 × ½) observed to be welded between the piles were also explicitly modeled, as they significantly increase the bent's lateral stiffness. In summary, the

SAP2000 model was a three-dimensional (3D) representation of the bent (including piles, cap, and bracing), although the analysis of its behavior was confined to the planar transverse direction of interest. In other words, the model captures the 3D geometry, but the research team examined the bent's response in the single transverse plane because the motion in that direction was the focus of this study.

The SAP2000 model of the bent (see figure 21) was used to compute the bent's lateral stiffness and to perform modal analysis. To represent the mass participation for the bent's transverse vibration mode, a tributary mass was assigned to the bent based on the portion of the superstructure it supports. Considering a tributary width of 40 ft of deck (half the span on each side of the bent because the girders are simply-supported at the bent), the total weight of the associated superstructure and substructure components was converted into an equivalent lumped mass. In the chosen units (kips and inches), this tributary mass was estimated to be about 1.88 kip·sec²/in.

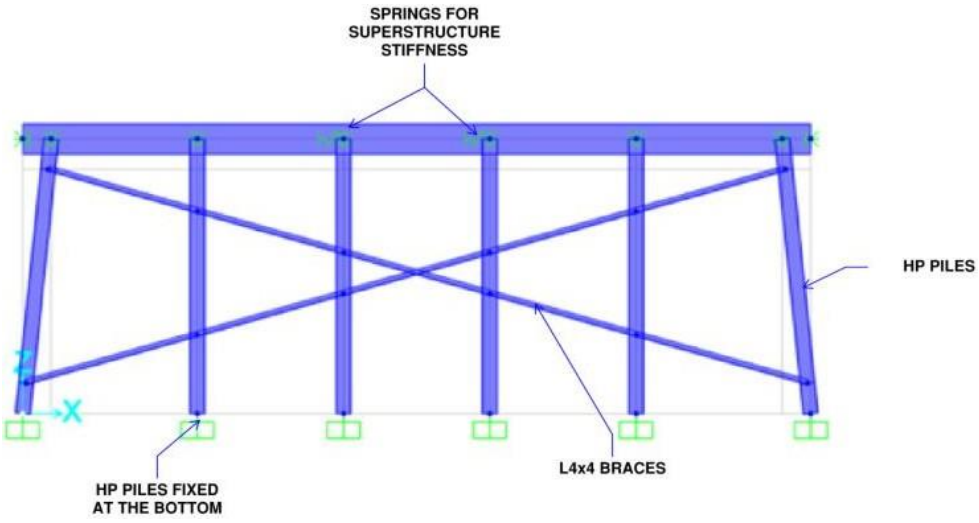

Figure 21. Diagram. Analysis model of the scour critical bent.

It is important to note that the superstructure was not explicitly modeled in the analysis. The spans on either side of the bent are separated by deck joints, and the girders are discontinuous at the support, effectively isolating the spans in terms of flexural continuity. Therefore, the stiffness contribution of the adjacent spans was excluded from the transverse vibration model. However, due to the presence of neoprene bearing pads, the superstructure is not entirely free to move laterally—some frictional resistance may develop at the bearings during small-amplitude vibrations. Although design practice typically assumes plain elastomeric bearings provide negligible lateral restraint, limited frictional resistance can occur in reality. Because this effect is difficult to quantify directly, it was idealized in the model as an equivalent lateral spring acting between the bent cap and the superstructure. The stiffness of this spring was not known a priori and was treated as a calibration parameter.

Using the field test results for guidance, the research team adjusted the stiffness of the superstructure spring in the model so that the combined system's natural frequency matched the observed 2.68 Hz. Through this calibration process, the lateral support at the bent was represented as two parallel springs acting in the transverse direction: (1) the bent (piles plus bracing) providing one spring, and (2) the effective contribution of the superstructure (through bearing friction and any other minor restraint) providing the second spring. The calibrated stiffness values were approximately 355 kips/in. for the bent itself and 180 kips/in. for the superstructure's effect. These in parallel give the overall lateral stiffness corresponding to the 2.68 Hz mode. Figure 22 illustrates the simplified single-degree-of-freedom (SDOF) idealization of the system: the bent and its tributary mass are modeled as an SDOF oscillator with a total lateral stiffness equal to the sum of the bent stiffness and the calibrated spring stiffness. This

calibrated model accurately reproduces the measured natural frequency and thus provides confidence in the estimated in situ stiffness of the bent.

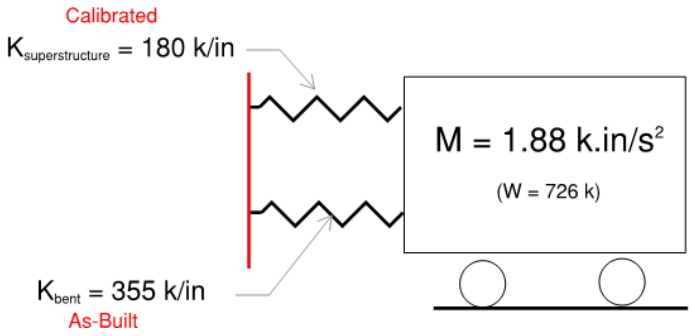

Figure 22. Diagram. Idealized mass and stiffness of the bent in the riverbed direction as an SDOF system.

SCOUR SIMULATION AND MACHINE LEARNING TRAINING DATA DEVELOPMENT

With a validated baseline model in hand, the next step was to investigate how potential scour would affect the bent's lateral stiffness and natural frequency. Scour was simulated in the SAP2000 model by incrementally increasing the unsupported length of the piles (i.e., reducing the fixity depth). In practical terms, this was done by lowering the point of fixity of each pile downward to reflect soil loss, effectively increasing the exposed pile length. Scour depths ranging from 0 to 7 ft were considered, in 1-ft increments. For each scour scenario, the cross-sectional properties of the piles remained the same, but the length of each pile above the new soil support level was longer, resulting in a reduction in lateral stiffness of the pile group. The steel bracing was kept in the model on the assumption that it remains intact and connected even if the water level drops, and the previously calibrated superstructure lateral spring (180 kips/in.) was kept constant for all scenarios. Scour was assumed to affect only the stiffness of the substructure (i.e., the piles), while the contribution of the superstructure remained unchanged.

For each simulated scour depth, a modal analysis (or an eigenvalue analysis) was performed on the bent model to compute the lateral stiffness of the bent and the corresponding fundamental frequency of the idealized SDOF system. As expected, the progressive removal of soil support (increasing scour depth) led to a decrease in lateral stiffness and a lower natural frequency. These results are summarized in table 6, which lists the bent's lateral stiffness and SDOF natural frequency for each assumed scour depth. The trend demonstrates that even moderate scour (e.g., 1–2 ft of exposure) can significantly reduce stiffness and frequency, highlighting the value of dynamic monitoring for early detection of scour impact.

Table 6. Stiffness and natural frequencies for increasing scour.

Scour depth (ft)	Bent Stiffness (k/in)	Superstructure Stiffness (k/in)	Total Stiffness (k/in)	Natural Frequency (Hz)
0	355	180	535	2.68
1	306		486	2.56
2	260		440	2.44
3	215		395	2.31
4	176		356	2.19
5	145		325	2.09
6	122		302	2.02
7	105		285	1.96

To support the development and training of the ML-based scour detection module, a comprehensive set of simulated response data was generated. Instead of relying on purely synthetic white noise excitations, the excitation functions were developed directly from the measured ambient vibration data collected at the site. This ensured that the scour scenario simulations were driven by loading functions that realistically represent the bridge's operating environment. The process included the following:

- **Filtering:** Raw acceleration signals were first filtered to remove spurious noise outside the expected vibration frequency range.
- **Integration:** The filtered accelerations were integrated to obtain velocity and displacement time histories.
- **Detrending:** Because the initial conditions of the field recordings are unknown, the velocity and displacement signals were detrended to eliminate artificial drifts introduced by integration.
- **Loading Function Development:** Using the filtered accelerations together with the detrended velocity and displacement time histories, realistic excitation functions were created. These are not identical to the original site excitations but represent low-amplitude, physically realistic inputs consistent with typical bridge vibration sources, such as ambient traffic, wind, and hydrodynamic effects.

By using these site-informed loading functions in place of idealized white noise inputs, the scour simulations more accurately reproduce the spectral content, amplitude range, and duration of actual bridge vibrations. This makes the resulting dynamic responses more representative of the signals expected in practice and better suited for ML model training.

A linear elastic time history analysis was then conducted for each scour scenario using a 2 percent critical damping ratio assumed for the structure. The response of the idealized SDOF system was simulated under each excitation type through numerical integration of the equations of motion. The resulting output included acceleration time histories and corresponding frequency spectra for each level of scour. Collectively, these simulations produced a comprehensive dataset of vibrational responses labeled according to scour depth, providing the necessary input for training the ML-based detection module.

These simulated response datasets were compiled to serve as training and validation data for the ML-based scour detection algorithm under development. By training the ML model on vibration signatures corresponding to known scour conditions (from 0 to 7 ft of scour), the system can learn to recognize patterns or shifts in the frequency content, amplitude, or other features that correlate with progressive scour. In the broader project, this ML module would continuously monitor incoming field data from the sensors on the bridge and compare it to the learned patterns, thereby providing an alert if the bridge's vibration characteristics begin to resemble those of a scour-compromised state. The field testing and modeling efforts described above form the foundation for this approach, ensuring that the ML model is grounded in both real-world measurements and robust structural simulations.

CHAPTER 7. MACHINE LEARNING MODEL

SCOUR DEPTH PREDICTION MODEL

A bridge's structural vibration response is a high-dimensional, nonstationary time-series signal influenced by hydraulic forces, traffic loading, environmental conditions, and inherent structural dynamics. Manually engineering features that reliably quantify scour depth from such raw vibration data are extremely difficult, if not infeasible, due to the complexity and nonlinear interactions among these factors. To address this challenge, a deep learning approach was adopted as an effective means of automatically extracting salient patterns and learning the underlying nonlinear relationships between pier vibration signatures and corresponding scour depth. This data-driven framework bridges the gap between raw sensor measurements and actionable structural health insights, enabling automated, resilient, and continuous scour monitoring. It is designed to robustly differentiate between operational conditions, such as flood versus non-flood conditions, thereby supporting early detection and improved decision-making for bridge safety.

Proposed Mixture of Experts (MOE)-Based Scour Depth Prediction Workflow

The core of the proposed predictive framework is a Mixture of Experts (MoE) architecture, which employs a "divide and conquer" strategy to enhance prediction accuracy and reliability. This approach is particularly effective for systems that exhibit distinct behavioral regimes, such as bridges subjected to varying hydraulic conditions. As illustrated in the workflow shown in figure 23, the process begins with a 10-second window of acceleration data acquired in real time along the river flow axis. This data segment is first passed through a gating network, which classifies the current hydraulic condition as either "flood" or "non-flood". The gating decision

then directs the data window to one of two specialized expert networks. Each expert model is trained exclusively on data corresponding to its designated regime, enabling it to learn the nuanced vibration-scour relationships unique to that condition. The selected expert processes the input vibration sequence and produces a single numerical estimate of scour depth. This design choice of the MoE architecture is intended to capitalize regime-specific learning, thereby enhancing the accuracy of scour depth predictions while also supporting efficient, scalable real-time inference.

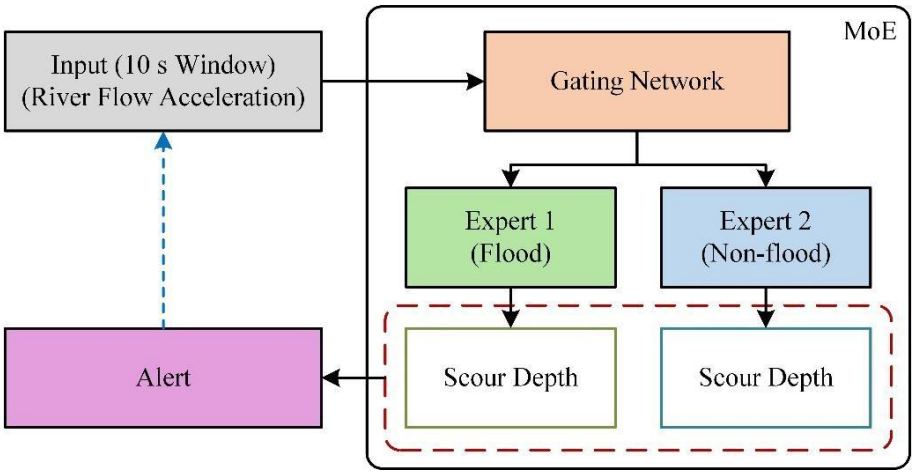

Figure 23. Flowchart. Proposed MoE-based scour depth prediction workflow.

Model Architecture

The MoE model consists of three components: a gating network and two architecturally identical expert networks, each trained under a distinct flow regime: flood versus non-flood conditions. The Gating Network (see figure 24) functions as a binary classifier responsible for identifying the current flow regime. Its primary components include:

- **Convolutional Layers:** These layers scan the raw vibration time-series data to automatically extract local patterns and discriminative features that distinguish flood or non-flood conditions.
- **Pooling Layers:** Following the convolutional layers, pooling layers are used to down-sample the extracted signals to reduce dimensionality and enhance robustness to noise and signal variability. This improves the model's generalizability across diverse operational conditions.
- **Fully Connected Layers:** These layers synthesize all the high-level features to make a final, definitive classification of the input signal as either "flood" or "non-flood".

Two Expert Networks (see figure 25), one for flood conditions and one for non-flood conditions, share an identical architecture but are trained on regime-specific data to capture nuanced vibration-scour relationships. Their architecture is similar to the gating network's but with a different objective:

- **Convolutional and Pooling Layers:** These layers extract deep structural features from the input vibration signals that are predictive of scour depth.
- **Output Layer:** Instead of classification, the final fully connected layer in each expert outputs a single continuous numerical value, representing the predicted scour depth.

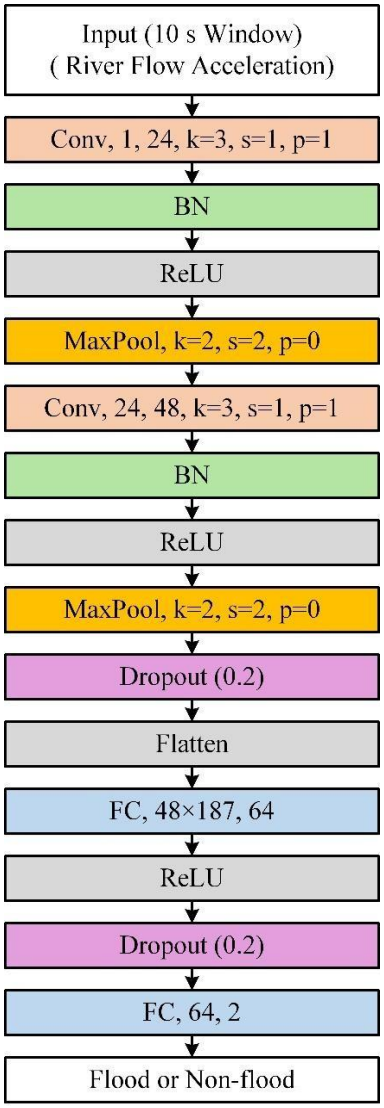

Figure 24. Diagram.
Gating network architecture.

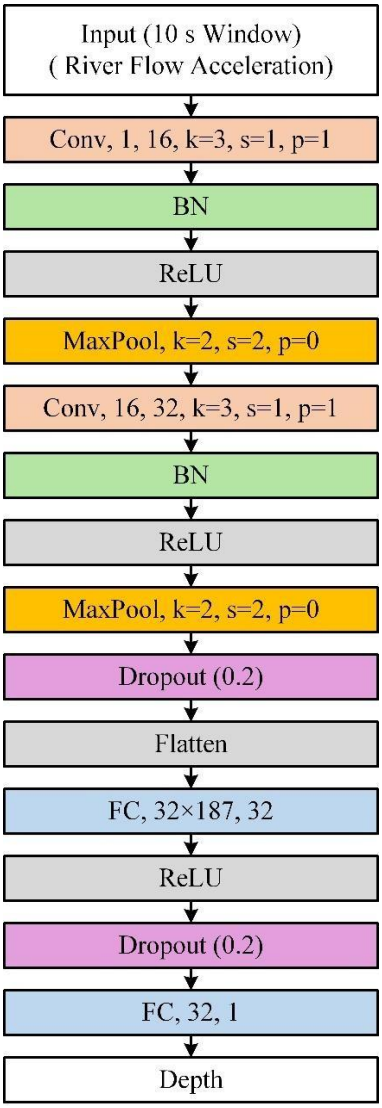

Figure 25. Diagram.
Expert network architecture.

Model Training

The model was trained using data acquired directly from the field deployment. This dataset consists of synchronized acceleration and scour depth measurements, ensuring the model's performance reflects true in-situ bridge behavior. A balanced dataset of 30,000 10-second data windows was compiled, containing 15,000 samples from flood conditions and 15,000 from non-

flood conditions. This dataset was partitioned into a training set (80%), a validation set (10%), and a test set (10%) to facilitate robust model development and evaluation.

A staged training strategy was adopted to ensure stable and efficient convergence. In the first stage (pre-training), the gating network and each expert network were trained independently on their respective tasks and regime-specific data subsets. This allowed each component to establish strong baseline representations. In the second stage (fine-tuning), the pre-trained modules were integrated into the full MoE architecture and jointly optimized for 80 epochs. The training was performed using the Adam optimizer. A dynamic learning rate schedule was employed, where the learning rate was halved if the validation loss did not show improvement for two consecutive epochs. This adaptive strategy helped prevent premature convergence and improved the model's overall predictive performance.

Performance Evaluation

The performance of the trained MoE model was evaluated on the independent test set, which the model had not seen during training. The model's convergence behavior is depicted in the loss curve (see figure 26). Both the training loss and validation loss decreased steadily over the course of training, eventually converge with minimal divergence between them. This pattern indicates that the model effectively captured the underlying patterns without exhibiting apparent overfitting.

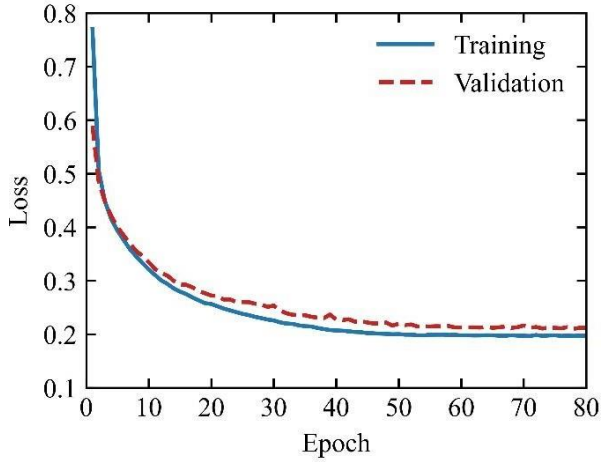

Figure 26. Graph. Training loss and validation loss of the MoE model.

The final model demonstrated strong performance on the test set, as follows:

- **Gating Accuracy:** The gating network, responsible for classifying each data window as either flood or non-flood, achieved an accuracy of 94.65%. This high accuracy ensures that the vibration data is correctly routed to the appropriate expert network for nearly all cases, which is essential for the overall effectiveness of the MoE framework.
- **Scour Depth Prediction RMSE:** The expert networks achieved a Root Mean Square Error (RMSE) of 0.37 ft for scour depth estimation. RMSE quantifies the average deviation between predicted and observed scour depths, demonstrating a high degree of precision for field monitoring purposes.

STRUCTURAL ANOMALY DETECTION MODEL

While the MoE model delivers high-precision predictions for scour depth, a comprehensive structural health monitoring framework requires a broader capability to detect a wider range of anomalous events beyond scour. The current scour prediction model is formulated as a supervised regression task, trained specifically to learn vibration patterns associated with scour

depths. However, bridges may experience other events, such as vehicular impacts, structural degradation, or unforeseen environmental loads, that can similarly influence their vibration signatures. Identifying these diverse anomalies requires additional analytical capabilities that extend beyond the scope of the existing scour-focused model.

Furthermore, the operational reliability of physical sensors, such as the sonar sensors for scour measurement, can be compromised under certain conditions. During non-flood periods with low water levels, these sensors may be exposed to air and fail to provide valid data. To address these limitations, we introduce a complementary unsupervised anomaly detection method for general-purpose system health monitoring. This approach identifies significant deviations from the established "normal" structural behavior. Designed for continuous operation, it provides an essential layer of safety, especially during non-flood periods, while remaining effective during flood events.

A key distinction in the data processing for this method is the use of a 30-second data window, as opposed to the 10-second window employed for scour prediction. This design choice is deliberate: anomaly detection relies heavily on frequency domain analysis to capture subtle changes in the structural dynamics. A longer, 30-second window enables higher frequency resolution in the Fast Fourier Transform (FFT), allowing for a more detailed and accurate characterization of the vibration spectrum. This enhanced resolution is essential for detecting small shifts in the pier's natural frequencies, which are often early indicators of changes in structural condition.

Proposed Anomaly Detection Workflow

The anomaly detection workflow is an unsupervised process that transforms raw vibration data into a binary judgment ("Normal" or "Abnormal"). The workflow proceeds as follows:

1. **Data Transformation to Frequency Domain:** Each 30-second window of raw acceleration data is converted into the frequency domain using a Fast Fourier Transform (FFT). This process yields the amplitude of vibration at discrete frequency intervals.

2. **Feature Vector Construction:** A 301-dimensional feature vector is constructed by extracting the FFT amplitudes within a frequency range pertinent to the pier's structural dynamics (approximately 0.67 Hz to 10.72 Hz). This vector serves as a unique "fingerprint" of the structure's vibrational state for that time window.

3. **Z-score Standardization:** Each feature vector is standardized using the pre-computed mean and standard deviation from a large dataset of normal operational data. This step normalizes the features, ensuring that each frequency component is weighted appropriately by the subsequent model.

4. **Unsupervised Model Inference:** The standardized Z-score vector is passed to a pre-trained Autoencoder model, which calculates a "reconstruction error." A low error indicates the data conforms to the learned normal patterns, while a high error suggests a deviation, signaling a potential anomaly.

Model Architecture

The core of this detection system is a 1D Convolutional Autoencoder, well suited for learning patterns in time-series and spectral data. As an unsupervised model, it is trained to learn or compress "normal" structural behaviors. The model consists of two main components:

- **Encoder:** The encoder's function is to compress the high-dimensional (301-dim) input feature vector into a low-dimensional latent representation, often called the "bottleneck". It achieves this through a series of convolutional and fully connected layers that progressively extract the high-level salient features of the input data. The architecture of the encoder is detailed in Figure 27.
- **Decoder:** The decoder has a symmetric, inverse architecture to the encoder. It takes the compressed bottleneck representation and attempts to reconstruct the original 301-dimensional input vector. It utilizes transposed convolutional layers to progressively up-sample the features back to their original dimension.

The fundamental principle is that the model learns to reconstruct the majority of samples in the training dataset. When presented with an anomalous input that deviates from the learned patterns, the model will struggle to reconstruct it faithfully, leading to a significantly higher reconstruction error (measured as Mean Squared Error).

Model Train and Threshold Setting

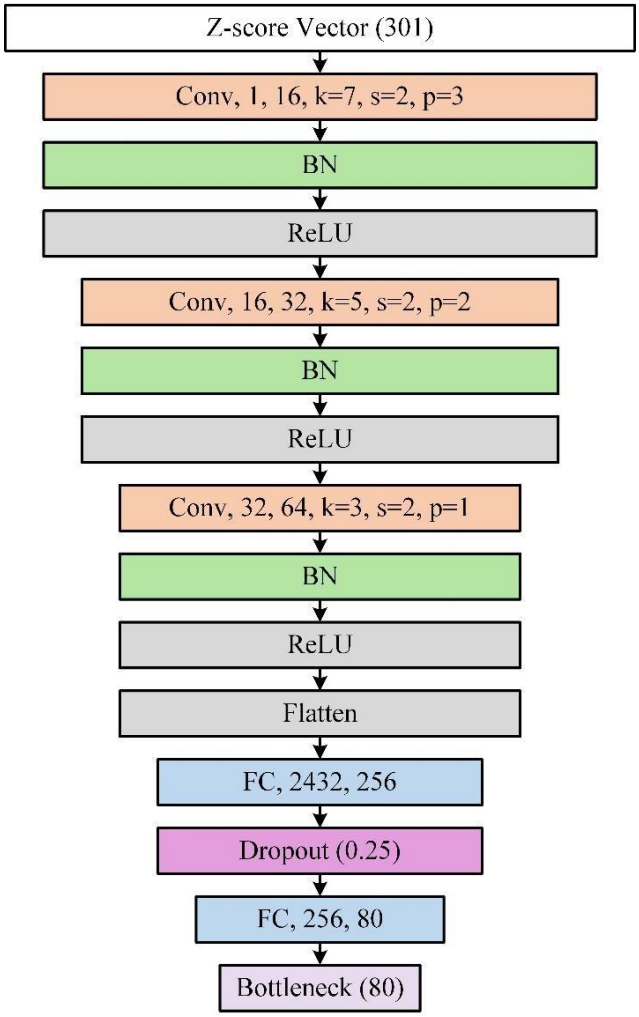

Figure 27. Diagram. Anomaly detection model encoder architecture.

The Autoencoder model was trained on a dataset of 12,752 samples, each representing a 30-second vibration window that includes both flood and non-flood periods. The dataset was split into a training set (80%) and a validation set (20%). The model was trained for 50 epochs using the Adam optimizer to minimize the Mean Squared Error (MSE) between the original input vectors and the outputs reconstructed by the decoder.

The model's convergence behavior is shown in figure 28. The training and validation losses decreased in tandem and converged eventually with a final validation loss of 0.602.

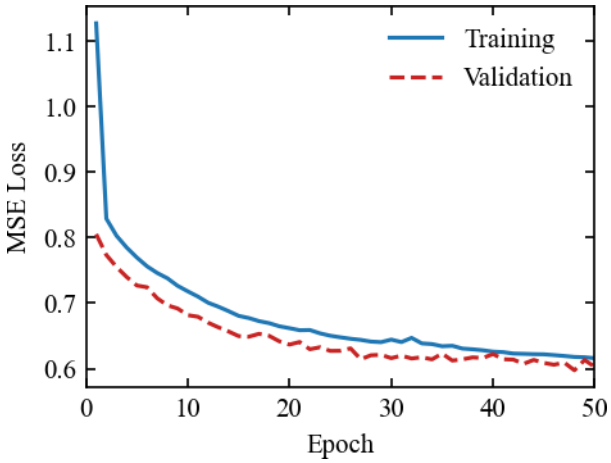

Figure 28. Graph. Training and validation loss of the autoencoder model.

Following successful training, an anomaly threshold was established. All 12,752 normal samples from the dataset were processed by the trained model to generate a distribution of their reconstruction errors. As shown in figure 29, the vast majority of normal samples yielded a low reconstruction error. To establish a robust decision boundary, the 99th percentile of this error distribution was selected as the anomaly threshold. This resulted in a threshold value of 1.45. In real-time operation, any data window producing a reconstruction error exceeding 1.45 is flagged as "Abnormal".

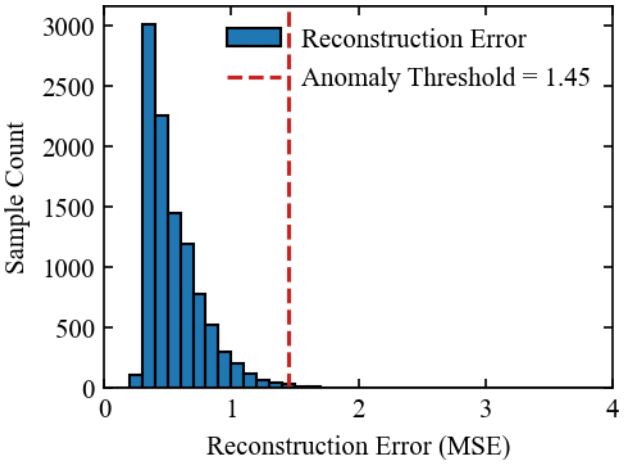

Figure 29. Chart. Distribution of reconstruction error and anomaly threshold.

CHAPTER 8. OPTIMIZATION MODELS

Part of the scope of this research is to produce an optimization algorithm for human resource allocations. Once the fully integrated system obtains warnings from BridgeWatch© and the field sensors, the optimization algorithm can be used to assign inspection teams to the various bridges in the most time-efficient manner.

Two optimization models were deployed to this system, namely, static optimization and route optimization. The purpose of the static optimization routine is to allow GDOT to optimize available inspection teams to complete the inspection job for the bridges that are flagged for a storm event. The static optimization routine utilizes travel time based on the existing highway speed limits and distances of one bridge to others. Route optimization provides the fine-level optimization. After inspection teams are assigned to the bridges, the user has the option to further produce vehicle route optimization using actual traffic and travel time data.

STATIC OPTIMIZATION

The bridge inspection assignment and routing problem were formulated as a mixed-integer programming (MIP) problem over multiple GDOT bases ("depots") and inspection teams. The goal is to: (1) minimize overall working time across teams and (2) balance the workload so no team is overloaded, subject to assigning every bridge exactly once and constructing consistent intra-team routes.

Static Optimization in Scour View

When the Static Optimization option is chosen within the Scour View website, the required input will show in a pop-up box, as shown in figure 30.

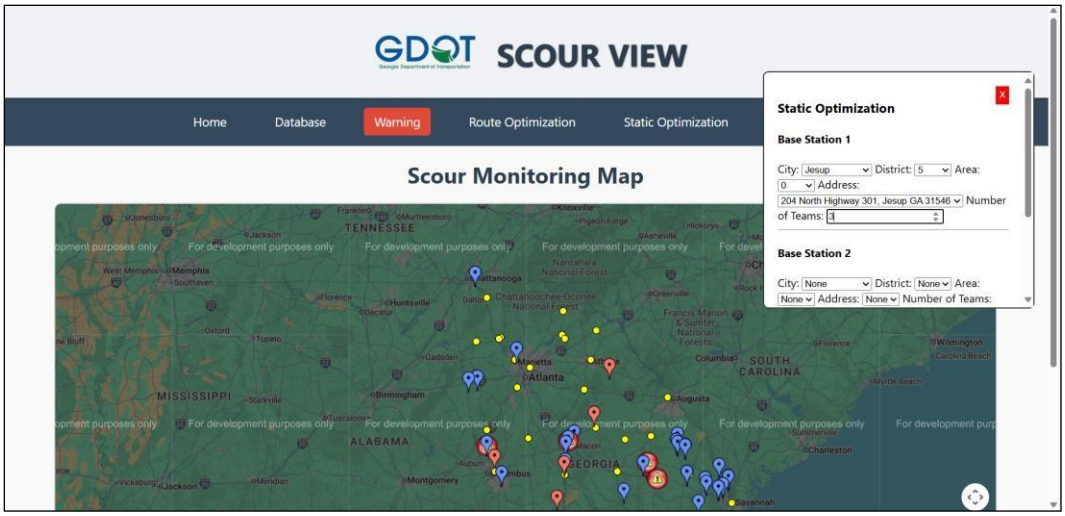

Figure 30. Screenshot. Input for the Static Optimization model on Scour View.

The input includes City of the base station(s) and Number of Teams in each base station. Other fields, such as the District, Area, and Address of the base stations, listed in the pop-up box are pre-populated options and can be chosen from the dropdown list. All of the information is needed for each base station. If more than one base station is desired, the user can opt to fill in the information for the second base station; otherwise, the Base Station 2 option can be left as is.

Once the fields are populated, the user can scroll down to the pop-up box and click on the "Run Static Optimization" button. This will execute the optimization algorithm. The results of the optimization algorithm are presented on the map as well as in text format below the map. An example of the optimization results is shown in figure 31.

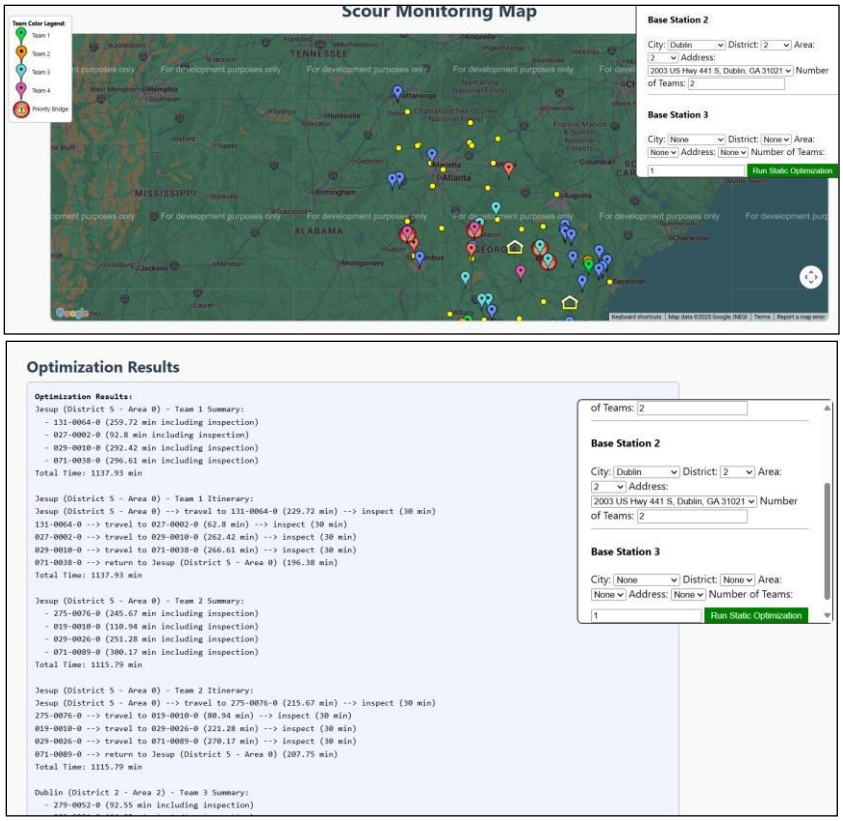

Figure 31. Screenshots. Map and text results of Static Optimization through Scour View.

Static Optimization Formulation

Because the Static Optimization routine uses "static" data of travel times based on highway speed and route lengths, two pairwise matrices were constructed. The first is a pairwise matrix that relates travel time from bridge to bridge. The second pairwise matrix relates the GDOT bases to the scour critical bridges. The pairwise matrices are then used to evaluate travel times between bridges and the GDOT bases.

The overall required datasets can be described as follows:

B = Set of bridges to inspect.

T = Set of inspection teams, where each team, t, is tied to a base, $s(t)$,

$$T,\ \ t\ \in T,\ \ s(t) \tag{1}$$

s > 0 = Per-bridge inspection time (minutes),

$$s\ >\ 0 \tag{2}$$

a[t,b] ≥ 0 = Travel time from team *t*'s base, *s*(*t*), to bridge, *b* (from site matrix),

$$a_{t,b}\ \geq\ 0 \tag{3}$$

r[t,b] ≥ 0 = Travel time from bridge, *b*, back to team *t*'s base, *s*(*t*) (from site matrix),

$$r_{t,b}\ \geq\ 0 \tag{4}$$

d[i,j] ≥ 0 = Bridge-to-bridge travel time from bridge *i* to *j* (from pairwise matrix),

$$d_{i,j}\ \geq\ 0 \tag{5}$$

$$N\ \ = |B|$$

The decision variables for Static Optimization are:

$x_{t,b} \in \{0,1\}$ = 1 if bridge *b* is assigned to team *t*; 0, otherwise.

$y_{t,i,j} \in \{0,1\}$ = 1 if team *t* visits *j* immediately after *i*; 0, otherwise (for i ≠ j).

$u_i \in [0, N]$ = Classic Miller–Tucker–Zemlin (MTZ) order variable used to prevent subtours.

$\tau_t \geq 0$ = Total working time of team *t* (travel + inspections + return).

$\tau \geq 0$ = Average team time.

$\delta_t \geq 0$ = Absolute deviation of team *t*'s time from the average.

The objective function was formulated as:

$$min\ \lambda \sum_{t \in T} \tau_t \ + (1 - \lambda) \sum_{t \in T} \delta_t \tag{6}$$

This objective function combines both the total time for all the teams to complete the inspection tasks as well as workload balance among teams, with weight of $\lambda = 0.7$ on total time and $1 - \lambda = 0.3$ on workload balance. These weights can be made adjustable depending on the emphasis of the optimization. The Mixed-Integer Linear Programming (MILP) technique is used to solve the objective function. As with all optimization problems, there are a set of constraints that are applied. These constraints are as follows:

1. **Coverage:** Every bridge is assigned exactly once,

$$\sum_{t \in T} x_{t,b} \ = \ 1\,, \ \ \forall\, b \ \in \ B \tag{7}$$

2. **Route Consistency (linking assignments and arcs):** For each team, if a bridge is assigned, exactly one outgoing and one incoming arc must be chosen among bridges,

$$\sum_{j \in B \setminus \{i\}} y_{t,i,j} \ = x_{t,i}\,, \sum_{j \in B \setminus \{i\}} y_{t,j,i} \ \ = \ x_{t,i}\,, \ \ \forall\, t \ \in \ T,\ \forall\, i \ \in \ B \tag{8}$$

3. **Subtour Elimination (MTZ):**

$$u_i \ - \ u_j \ + \ N \cdot y_{t,i,j} \ \leq \ N \ - \ 1\,, \ \ \forall\, t \ \in \ T,\ \forall\, i \ \neq \ j \in \ B \tag{9}$$

   Where, $0 \leq u_i \leq N\,, \forall\, i \in B$

4. **Team Time Accumulation:** Each team's time aggregates base-to-first legs + on-route travel + per-bridge inspections + last-to-base return. In the current implementation,

outbound and return times are tallied per assigned bridge (a star-approximation of base legs), and bridge-to-bridge legs are captured by *y*:

$$\tau_t = \sum_{b \in B} x_{t,b}(a_{t,b} + s) \quad + \sum_{i \neq j} y_{t,i,j}\, d_{i,j} \quad + \sum_{b \in B} x_{t,b}\ r_{t,b}, \quad \forall\, t \in T \tag{10}$$

5. **Average Time and Absolute Deviations:**

$$\tau \ = \frac{1}{|T|} \sum_{t \in T} \tau_t \tag{11}$$

Where, $\delta_t \geq \tau_t - \tau$; $\delta_t \geq \tau - \tau_t$, $\forall\, t \in T$

This encodes δ_t = |τ_t − τ̄| via linear inequalities.

This algorithm is all packaged in the system and will execute after input are provided. From the Scour View website, are only a few inputs are required to use this feature. The majority of the input described above were pulled directly from the warning system.

ROUTE OPTIMIZATION

The research team formulated the proposed Vehicle Routing Problem with Time Windows and Technician Constraints (VRPTW-TC) as an MIP to assign vehicles and maintenance crews to critical bridge sites across Georgia. The objective is to complete the required maintenance work in the minimum possible time using the available vehicles and technicians. The platform leverages Google Maps APIs for routing and real-time travel time data, and employs OR-Tools to solve the underlying optimization problem.

Route Optimization Objective Function

Let the network of maintenance locations be denoted by $N = \{0, 1, \dots, n\}$, where node 0 represents the GDOT base location, and let K be the set of available vehicles. The objective of the proposed VRPTW-TC is to minimize the total arrival time, T, at all maintenance-required locations, encouraging prompt service execution:

$$\min_{x_{ijk}, t_{ik}, u_k} T = \sum_{i \in N \setminus \{0\}} \sum_{k \in K} t_{ik} \tag{12}$$

Where,

$x_{ijk} \in \{0,1\}$ = A binary decision variable equal to 1 if vehicle k travels from location i to location j, and 0 otherwise.

$u_k \in \{0,1\}$ = A binary decision variable equal to 1 if assigned for maintenance work in optimal solution, and 0 otherwise.

$t_{ik} \in R_+$ = Time at which vehicle k arrives at location i.

Route Optimization Constraints

The constraints for route optimization are the following:

1. **Visit Constraints:** Each location requiring maintenance must be visited exactly once:

$$\sum_{k \in K} \sum_{j \in N, j \neq i} x_{ijk} = 1, \ \ \forall i \in N \setminus \{0\} \tag{13}$$

2. **Time Window Constraints:** Each location must be visited within the required maintenance time window:

$$e_i \leq t_{ik} \leq l_i, \ \ \forall i \in N \setminus \{0\}, \forall k \in K \tag{14}$$

Where, e_i is the lower bound and l_i is the upper bound of maintenance time window for location i.

3. **Technician Constraint:** The total number of technicians required by the assigned routes must not exceed availability:

$$\sum_{k \in K} \left(\max_{i \in \text{Route}_k} r_i u_k \right) \leq C \tag{15}$$

Where, r_i denotes the number of technicians required at location i.

4. **Time Propagation Along Routes:** The arrival times at each location must be consistent with travel and service times along the route taken by a vehicle to prevent "teleporting" or "arrive early":

$$t_{jk} \geq t_{ik} + s_i + d_{ij} - \text{M}(1 - x_{ijk}) \; \forall i, j \in N, \forall k \in K \tag{16}$$

Where,

s_i = Maintenance duration at location i.

d_{ij} = Real-time travel time from location i to location j retrieved from Google Maps.

M = A large constant (Big-M) used to ensure that the corresponding constraint becomes non-binding when vehicle k does not travel from location i to location j.

5. **Vehicle Flow Conservation:** This constraint ensures that each vehicle maintains a continuous, logical route (i.e., what goes in must come out) and there is no teleporting or disappearing mid-route:

$$\sum_{j \in N} x_{ijk} - \sum_{j \in N} x_{jik} = 0 \; \forall k \in K, \forall i \in N \tag{17}$$

Route Optimization Interface and Guide

This section provides a walkthrough of the Route Optimization option, which enables efficient scheduling and routing of vehicles and technician teams to bridge sites across Georgia by solving a VRPTW-TC. Users interact with the platform through a browser-based interface (see figure 32) built with Streamlit and powered by Google Maps APIs and Google OR-Tools.

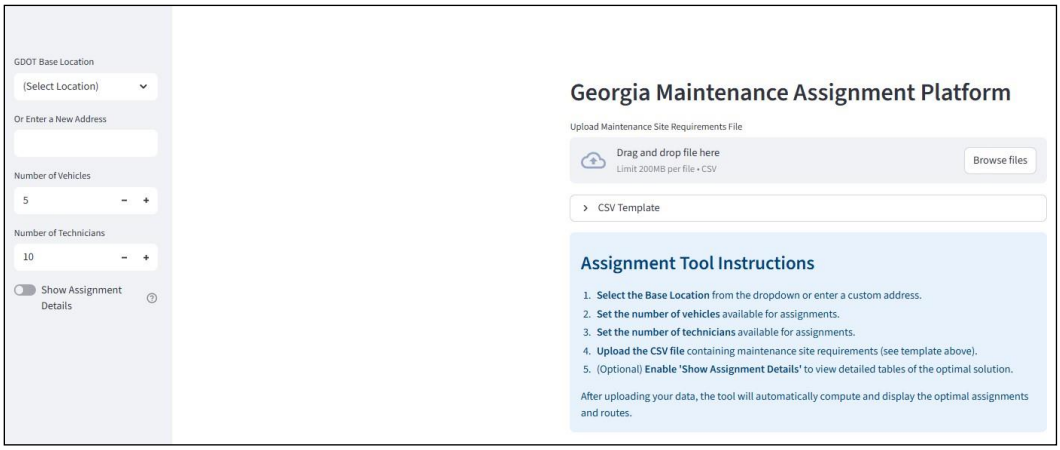

Figure 32. Screenshot. Route Optimization interface.

The process begins with the user defining a base location. This origin point can either be selected from a dropdown menu containing preloaded GDOT district facilities (see figure 33) across Georgia or entered manually in the text box labeled “Or Enter a New Address” (see figure 32).

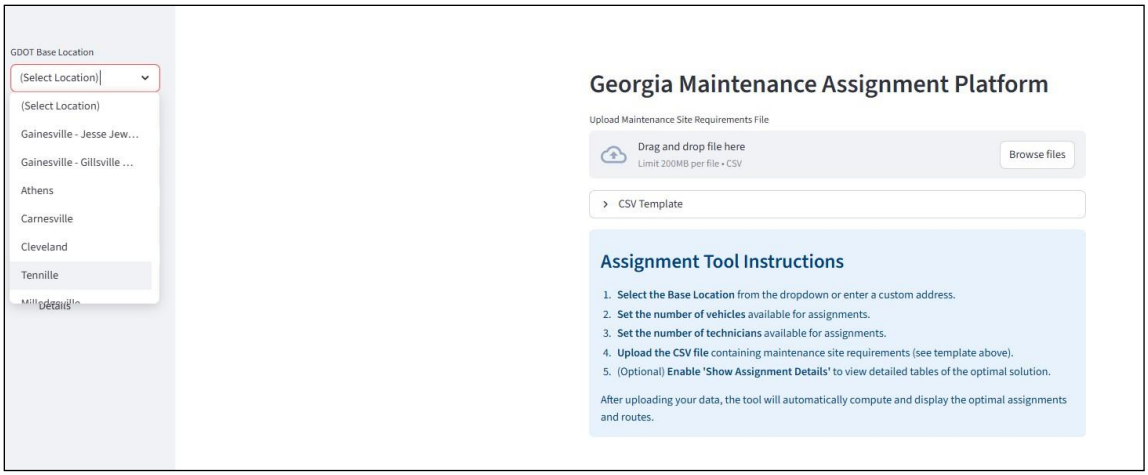

Figure 33. Screenshot. Dropdown box of input.

The tool then geocodes the selected or entered location using the Google Maps API and uses it as the anchor point for all vehicle routes. After establishing the base, the user specifies resource constraints in the sidebar, including the number of vehicles available for routing and the total number of technicians across all routes (see figure 34).

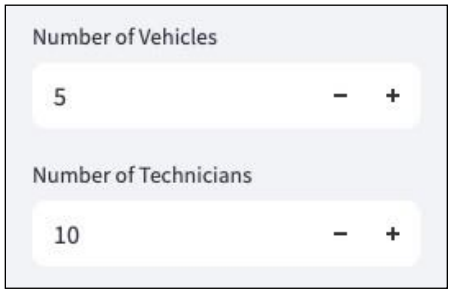

Figure 34. Screenshot. Input for number of vehicles and number of technicians for Route Optimization.

These inputs restrict the solution space, ensuring that the optimization remains operationally feasible by preventing assignments that exceed fleet or workforce capacity.

To populate the problem with real-world tasks, the user uploads a CSV file containing details for each potential bridge affected by the storm. The file must include required columns such as

latitude, longitude, maintenance status (0/1), earliest and latest allowable service times, number of technicians required, and service duration in minutes. Optional fields such as structure number, county, or facility carried by the structure may also be included for display purposes. Only sites marked with “Needs Maintenance = 1” are considered in the optimization, and a sample template is provided within the interface to assist in preparing the file.

Once a valid dataset is uploaded, the optimization process begins automatically. The system geocodes each maintenance location using its latitude and longitude or address, constructs a full travel time matrix via the Google Maps Distance Matrix API, and builds a routing model that incorporates all defined constraints. These include site-specific time windows, on-site service durations, technician requirements, and the availability of vehicles and the overall technician pool. The objective function minimizes the sum of arrival times at maintenance sites, with penalties applied for late arrivals. The solver iteratively searches for the minimum number of vehicles required to complete all tasks without exceeding technician availability. This process is fully automated and requires no further user input after the file is uploaded.

If a feasible solution is found, the interface displays a success message confirming completion of the optimization. Users are then presented with an interactive map that illustrates all vehicle routes using distinct color-coded paths, directional arrows, and labeled stops (e.g., Base, 1, 2, etc.). Each color corresponds to a specific vehicle assignment. For greater detail, the user may also enable a tabular route view, which presents stop order, location names, arrival and departure times, required technicians, service durations, and associated time windows. Together, the map and tables provide a complete overview of the optimized operational plan.

Although direct exporting is not yet integrated into the user interface, the tabular route assignments remain accessible through Streamlit's interactive tables. These can be manually copied or downloaded using the export button for external reporting and analysis.

In addition to route generation, the platform provides built-in diagnostic feedback to assist users in resolving common errors. If the uploaded CSV file does not contain any rows marked with "Needs Maintenance = 1," the system displays the message "*No locations require maintenance in the uploaded file.*" Users must ensure that at least one location is flagged for service. Geocoding errors may also occur, particularly if the base address cannot be converted into geographic coordinates or if coordinate strings are entered in an unrecognized degrees/minutes/seconds (DMS) format. In such cases, the system issues messages such as "*Could not geocode base address: [address]*" or "*Could not parse coordinates: [address]*," prompting users to verify address formatting and coordinate notation. Connectivity errors within the road network may arise when certain sites are unreachable due to invalid coordinates, isolated rural locations, or geocoding failures. Corresponding alerts, such as "*Some locations are unreachable by road*" or "*No route found between [location A] and [location B]*," guide users to review and correct problematic entries.

Optimization failures are also clearly indicated. If constraints are too restrictive—for example, overly tight time windows, insufficient vehicles or technicians, or sites that are geographically isolated—the solver may be unable to find a solution. In such cases, the message "*No solution found!*" is displayed. Errors may also occur during map visualization when decoding the polylines returned by the Google Maps Directions API. Warnings such as "*Overview polyline … could not be decoded. Trying step-by-step polylines*" or "*Directions API returned an error string*

... showing straight line" indicate fallback rendering strategies, with the system still displaying a line for continuity even when route data are incomplete.

To reduce errors, users are advised to ensure that time fields in the Earliest and Latest columns follow the 24-h (hh:mm) format, all numeric inputs such as *Technicians Required* and *Duration (min)* contain valid positive integers, and no mandatory fields are left blank for rows marked as needing maintenance.

The platform relies extensively on the Google Maps Platform (GMAP) to perform geocoding, routing, and visualization tasks, requiring a valid Google Maps API key. Keys are generated within the Google Cloud Console under *APIs & Services → Credentials* and should be restricted to approved referrers or IP addresses for security. Several APIs must be enabled in the same project, including the Maps JavaScript API, Geocoding API, Distance Matrix API, Directions API, Roads API, and, if needed, the Places API. These services collectively support map rendering, coordinate conversion, distance and travel time calculation, road snapping, and optional autocomplete functionality.

Google Maps services require billing to be enabled on the associated Cloud account. Free-tier usage covers a limited quota (e.g., 40,000 requests per month for the Geocoding API); however, charges apply beyond these thresholds. Budget alerts may be configured in the Cloud Console to prevent unexpected costs. For secure deployment, API keys should never be hardcoded into public repositories; instead, they should be stored in environment variables or secret-management tools, with appropriate restrictions applied. Within the application code, the key is referenced using the assignment gmaps_api_key = 'YOUR_API_KEY_HERE'.

CHAPTER 9. SCOUR VIEW WEB INTERFACE AND WARNING SYSTEM

At the front end, a dedicated website—currently named Scour View—was developed to serve as the primary user interface for the scour monitoring system. The platform provides both visualization of raw and processed data and remote control of system functionality, including the activation of different operational modes. Core functions of the Scour View web interface include the following:

- Monitoring data from scour critical bridges equipped with the sensor system.
- Providing a dashboard to visualize bridges affected by BridgeWatch© warnings.
- Enabling remote control of the sensor system to switch between operational modes.
- Supporting team allocation assignments during storms for bridges flagged for potential scour activity (see figure 35).

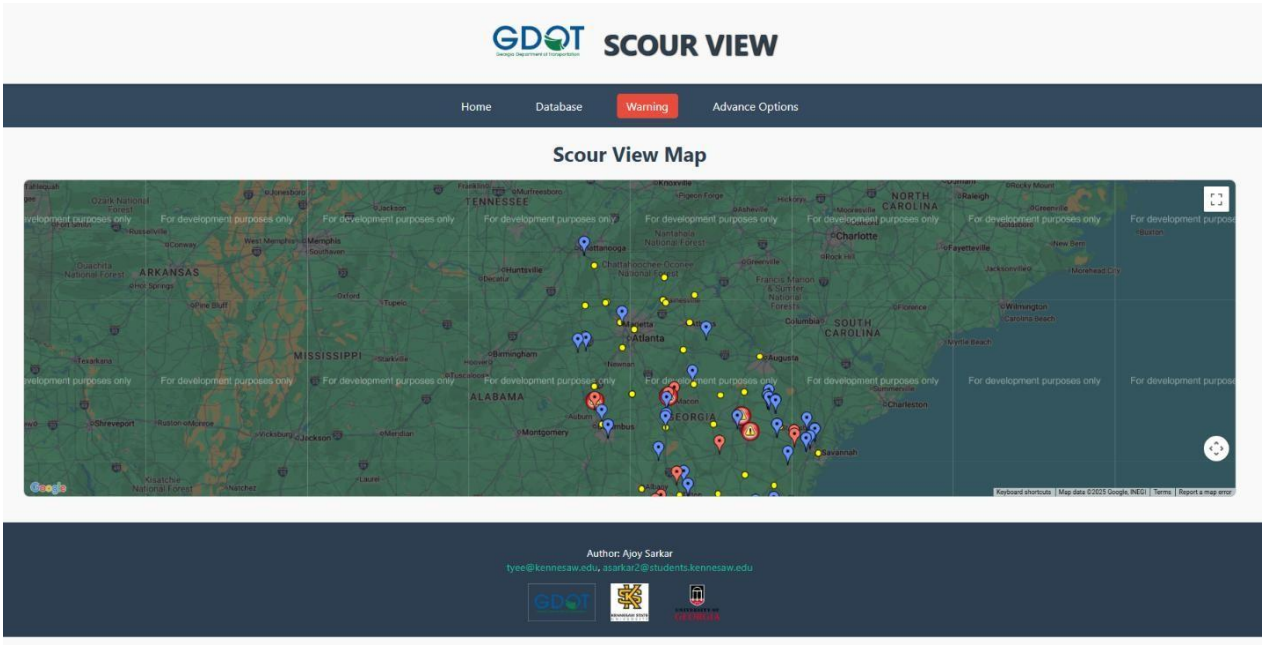

Figure 35. Screenshot. Scour View web interface.

MAP INTERFACE

Upon launch, the interface displays a map view zoomed to include all listed scour critical bridges. These bridges are preloaded from a CSV file stored on the Amazon Web Services (AWS) server, which can be periodically updated. Each bridge is represented as a blue marker on the map. The web interface operates in conjunction with a local email server to identify and display bridges affected by storm conditions. When the backend server receives updated information from BridgeWatch©, a compiled list of impacted bridges is transmitted to the web server. When received, the Warning tab on the website flashes red (see figure 35), prompting personnel to review the list of affected bridges displayed below the map.

STORM RESPONSE WARNING AND PRIORITY BRIDGE FEATURES

During storm events, data provided by BridgeWatch© are integrated in real time. Map markers corresponding to bridges under alert change color from blue to red, highlighting their at-risk status (see figure 36). For bridges equipped with the custom sensor system, continuous monitoring mode is automatically activated under high-flow conditions. In this mode, accelerometers and depth sensors collect high-frequency vibration and scour data.

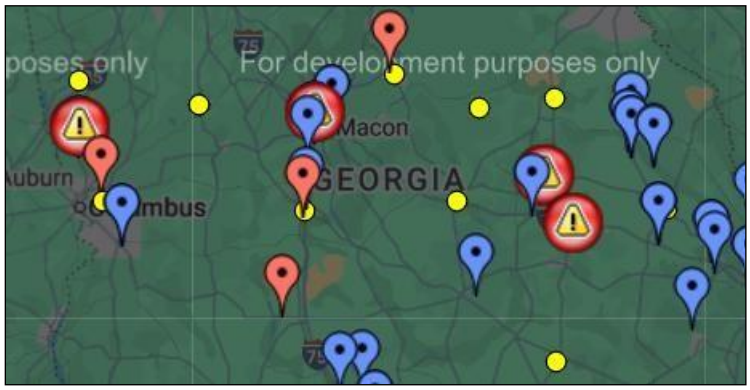

Figure 36. Map. Caution symbols indicating priority bridges.

If abnormal conditions are detected, the affected bridge is flagged as a priority bridge, and its marker icon changes to a caution symbol (a triangular icon with an exclamation mark), as shown in figure 36. Abnormal conditions may include the following:

- Excessive scour depths measured by the field-deployed sonar sensor.
- Significant discrepancies between predicted and measured scour depths.
- Anomalies in vibrational patterns.

During low-flow conditions, when scour may be masked by sediment deposition, vibrational anomaly detection becomes the primary monitoring method. This approach uses ML models trained on historical data collected during these frequent low-flow periods. By contrast, during high-flow (flood) events, a different ML algorithm—described in chapter 8—is applied to interpret vibrational data in combination with sonar depth measurements.

A user-specified threshold value, α, is assigned for each bridge based on inspection reports and post-installation field measurements. The warning system is triggered when either the ML-based scour depth inference or the direct sonar measurement exceeds this threshold. Figure 37 illustrates the conditions that activate the warning system.

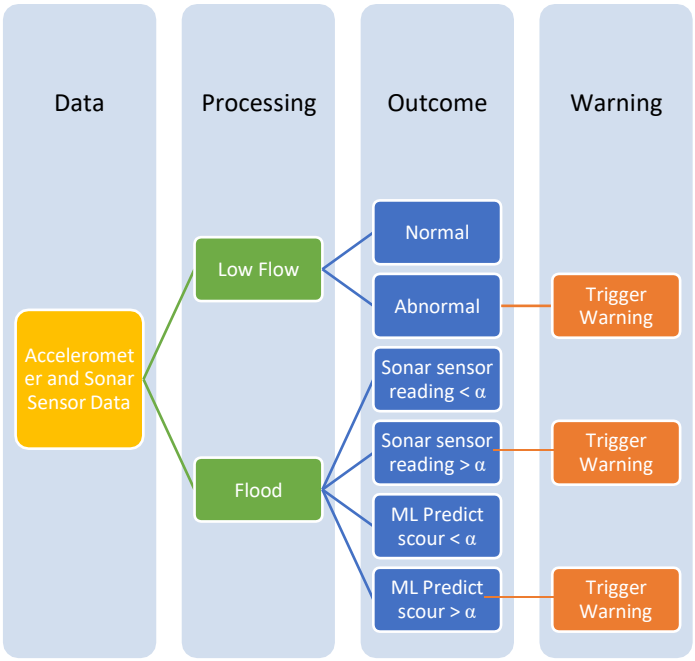

Figure 37. Flowchart. Conditions that will trigger a warning for the system.

EMAIL WARNING SERVICE

The warning system extends beyond the flashing Warning tab. An integrated email alerting service automatically notifies designated personnel when abnormal conditions occur, ensuring that critical information is communicated rapidly for timely decision-making and emergency response.

For proof of concept, the website is configured to refresh every 5 min to display the 10 most recent data entries. During storm events, when sensors collect data at high frequency, the backend continuously streams data to the web server and database. The user can adjust the refresh interval to provide more frequent updates as required.

DATA MAINTENANCE

To support long-term data management, Scour View includes a Database tab (see figure 35) that allows authorized GDOT personnel to review, download, and manage field data. This

functionality is intended to reduce storage costs within the AWS environment. Because deleted data cannot be recovered, best practice requires that backups be downloaded before removal.

ADVANCED OPTIONS

An Advanced Options tab (see figure 35) provides secure remote control of sensor operational modes and supports optimization of inspection team assignments during storm events. Access to this tab is password-protected and restricted to select individuals—such as the State Bridge Inspection Manager or State Bridge Maintenance Engineer—to safeguard system integrity and ensure that control over operations and resource allocation remains limited to authorized decision-makers.

CHAPTER 10. FIELD DATA AND RESULTS

Two remote monitoring systems were assembled and installed at two bridge sites, hereafter referred to as System 1 (Bridge 1) and System 2 (Bridge 2). Each system was equipped with four sonar scour sensors mounted on the leading bent, which experiences the greatest hydrodynamic forces during high-flow conditions and is therefore most vulnerable to scour. Sensors were positioned around the leading pile (i.e., the first pile in the direction of flow) to measure scour depths at multiple orientations. For smaller piles, scour depth is expected to be relatively uniform; therefore, the four-sensor configuration also provides redundancy, ensuring data continuity in the event of individual sensor malfunction (see figure 38).

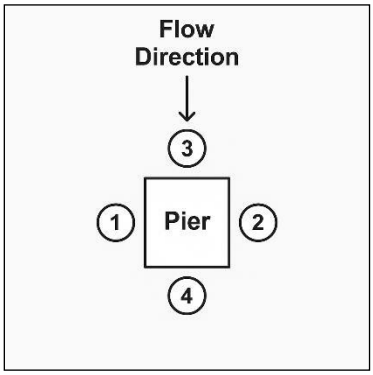

Figure 38. Diagram. General placement of sonar sensor relative to the stream flow direction.

Vibrational monitoring was achieved using accelerometers housed in transmitter boxes mounted above the bent caps. This placement enabled accurate sensing of structural vibrations while protecting the transmitter units from unauthorized interference (see figure 39).

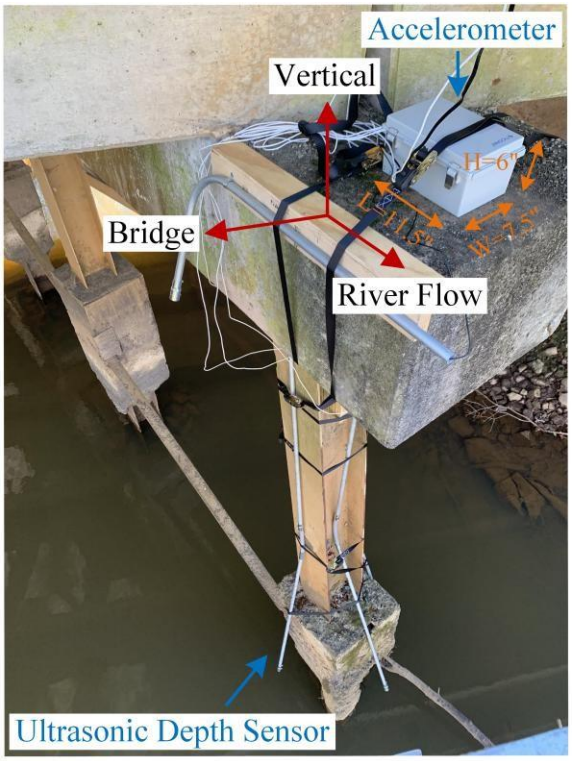

Figure 39. Photo. Completed transmitter installation, Bridge 1.

In addition to the two field installations, a duplicate system was maintained in the laboratory for continuous testing, troubleshooting, and demonstration purposes.

FIELD VALIDATION

Field validation was conducted at both bridge sites using a loaded truck to generate controlled vibrations. Braking maneuvers were performed at multiple points across each bridge to excite longitudinal (perpendicular to flow) and lateral (parallel to flow) responses. The objective was to characterize each bridge's natural frequency in both directions, providing essential parameters for structural modeling and backend analysis.

Acceleration data were recorded at multiple bents, including the scour critical bent and adjacent bents A and C (see figure 40).

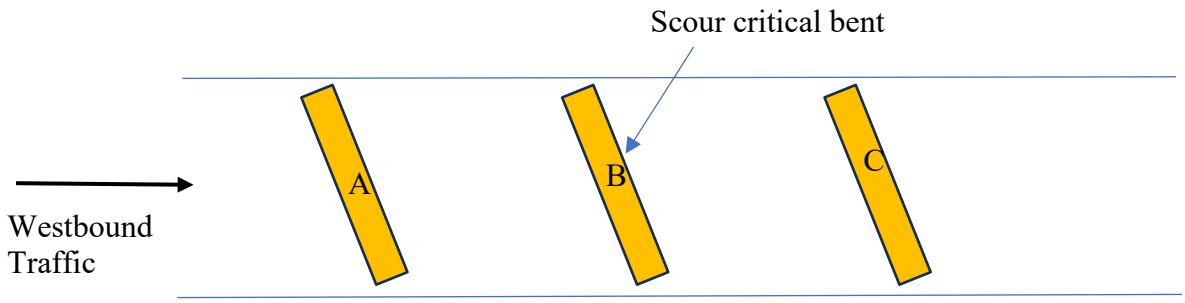

Figure 40. Diagram. Location of brake test on bridges relative to scour critical bent.

Short-Time Fourier Transform (STFT) analysis revealed dominant frequencies consistent across multiple tests. For example, a longitudinal braking event at Bridge 1 produced a peak response of approximately 2.1 Hz (see figure 41 and figure 42).

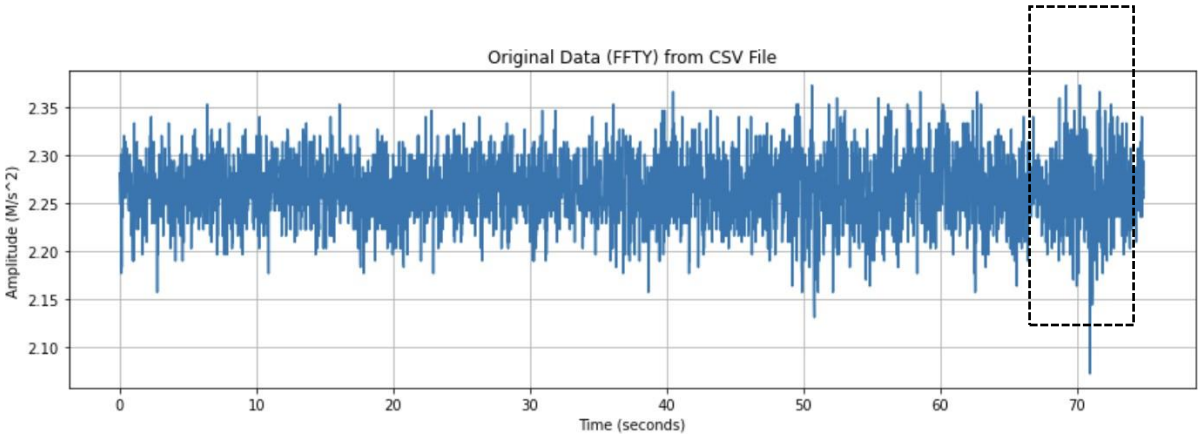

Figure 41. Graph. Longitudinal truck pulse event, Bridge 1, Acceleration 1.

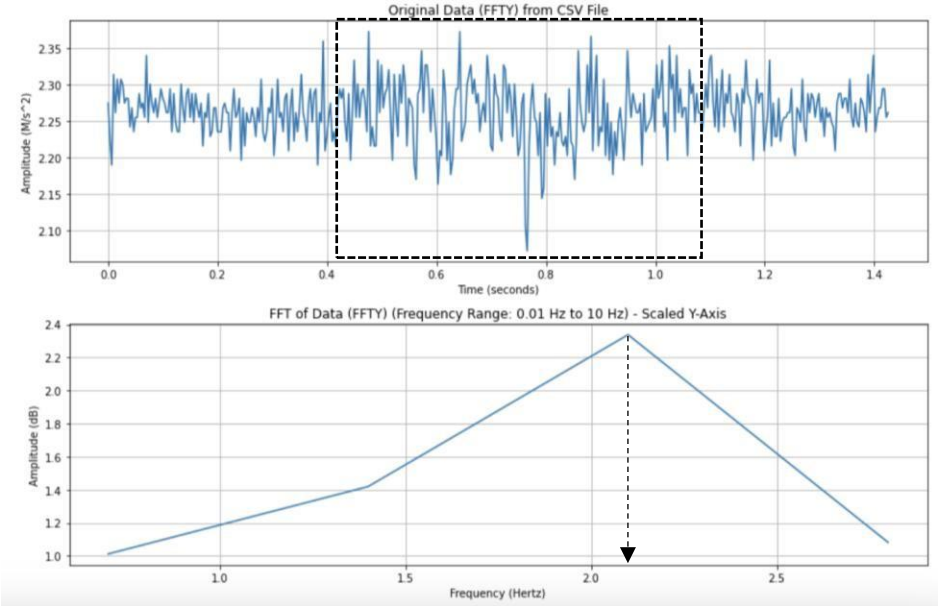

Figure 42. Graphs. STFT longitudinal truck pulse event output, Acceleration 1.

Results for all tests, which show strong agreement with the structural analysis expectations, are summarized in table 7.

Table 7. Summary brake test results for both bridges.

Bridge	Longitudinal/Lateral	Bent	Dominant Frequency (Hz)
1	Longitudinal	A	2.10
1	Longitudinal	B	2.20
1	Longitudinal	C	2.30
1	Lateral	A	2.80
1	Lateral	B	2.70
1	Lateral	C	2.65
2	Longitudinal	A	2.00
2	Longitudinal	B	1.90
2	Longitudinal	C	2.00
2	Lateral	A	2.60
2	Lateral	B	2.60
2	Lateral	C	2.60

Validation of the sonar probes was also performed. Surface water level sensors measured the distance from the bent cap to the water surface, which was confirmed against field measurements and design drawings (see figure 43).

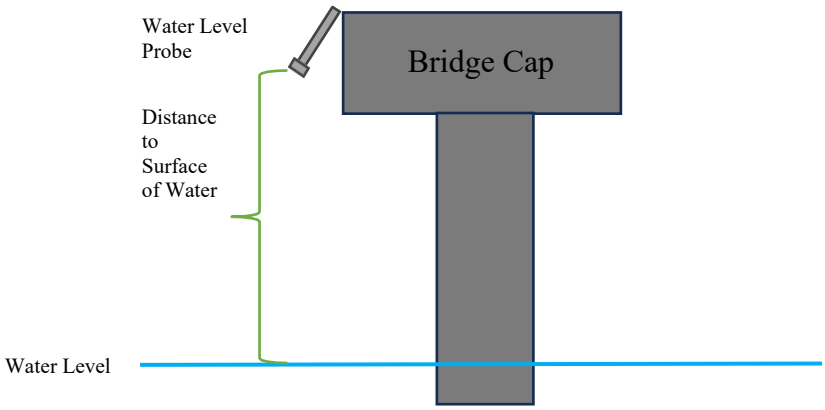

Figure 43. Diagram. Water level probe reading to river water level model.

Underwater sonar sensors, installed around the pier, recorded baseline depths of approximately 3.5 ft to the riverbed foundation, consistent with physical measurements. These values served as benchmarks for identifying scour-related bed elevation changes during flooding events (see figure 44).

Baseline Ambient Data (No-Flood Conditions)

Prior to major storm events, baseline vibration data were collected to establish baseline conditions. Ambient monitoring provided insight into bridge responses under low-flow conditions, where structures typically resonate at their natural frequency. Deviations from this baseline frequency serve as early indicators of structural changes, including scour or other health concerns.

Short bursts of ambient data were analyzed using STFT on the x-axis accelerations. Results consistently showed dominant frequencies of approximately 2.5–3.0 Hz, in agreement with the

truck brake test results. Representative time histories and frequency spectra are shown in figure 45 and figure 46.

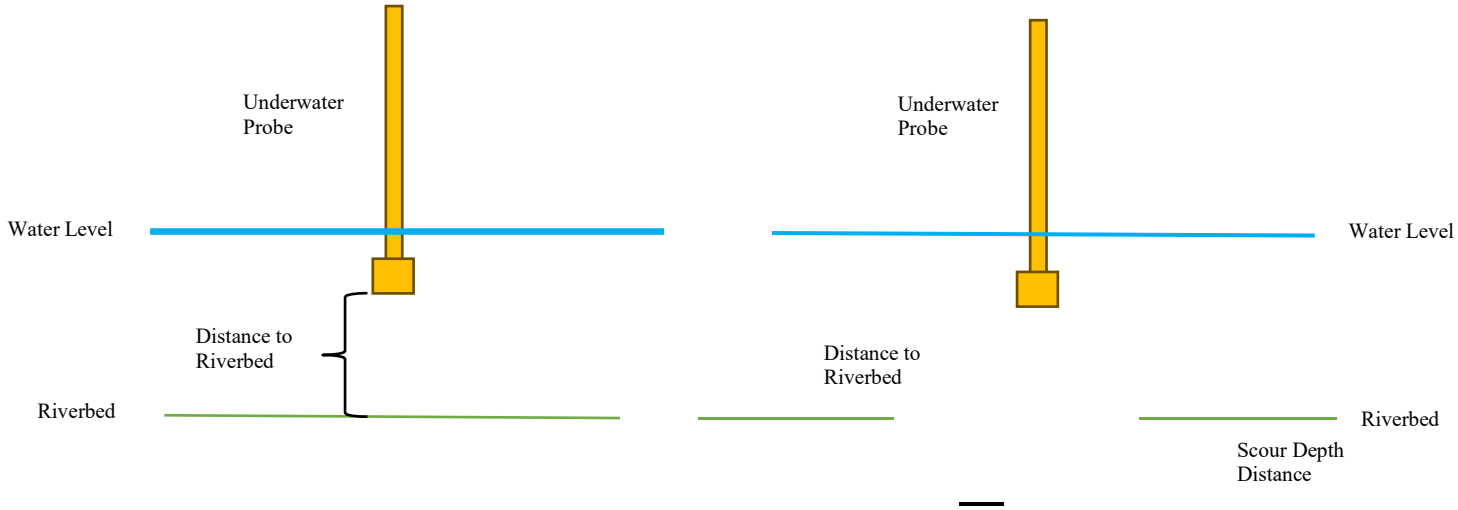

Figure 44. Diagram. Underwater probe sounding to river water level model.

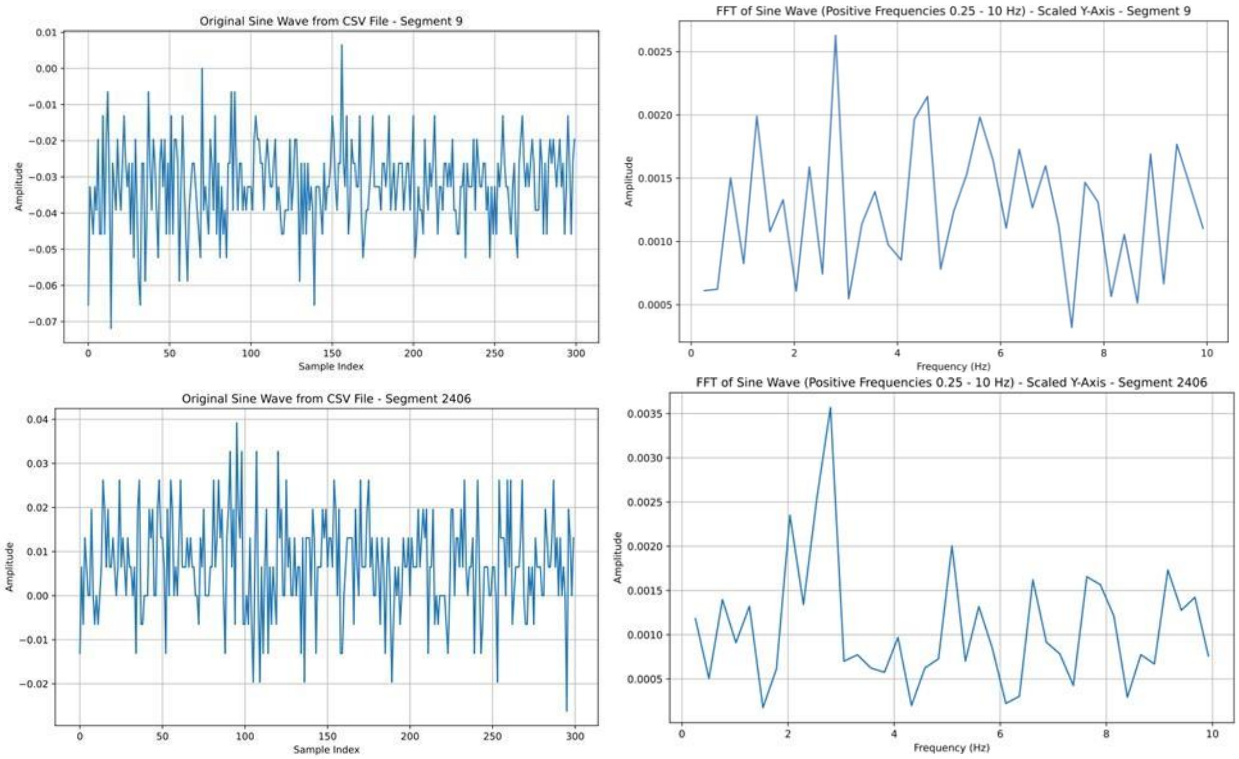

Figure 45. Graphs. Baseline acceleration samples with STFT outputs.

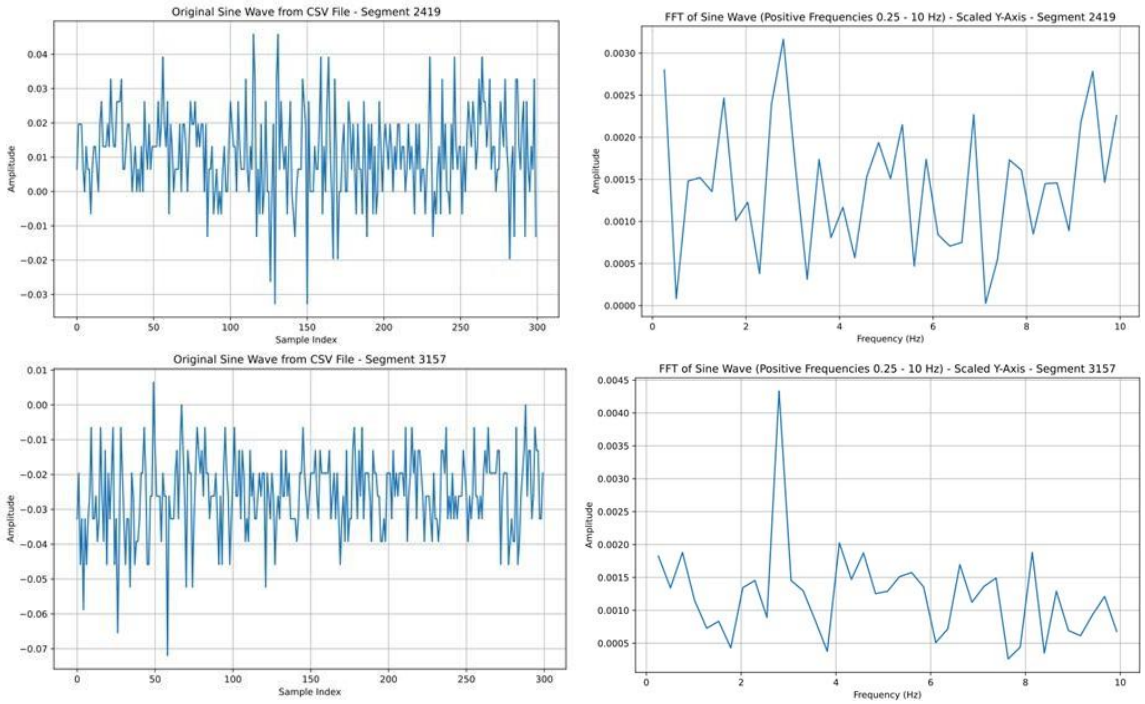

Figure 46. Graphs. No-flooding conditions acceleration samples with STFT outputs.

ANALYSIS OF LOW-FLOW OR AMBIENT DATA CONDITION (NO-FLOOD CONDITION)

The data collection started with baseline data collection. The purpose of the baseline data collection is to observe ambient vibration samples throughout the day for monitoring during no-flood conditions. Vibrational signals are expected to differ during high-flow versus low-flow scenarios and, therefore, health-monitoring techniques for both these conditions will also differ. Under this condition, the bridge will tend to vibrate at its natural frequency. Vibrational characteristics that deviate from the natural frequency are a good indicator of a shift in bridge health, regardless of whether it is a scour-related issue or not. Therefore, establishing and confirming the baseline ambient vibration under no-flooding and normal conditions is an essential part of this study.

Four short bursts of ambient data collected from using the sensor system over several days were separated and analyzed using the STFT. Only acceleration in the x-axis (i.e., river flow direction)

was used. Analysis results from the ambient data indicated that the natural frequency of the bridge is approximately 2.5 - 3.0 Hz, which again agrees with the results obtained from the brake tests. An example of the ambient data and the accompanying outcome of the STFT analysis is shown in figure 47 and figure 48.

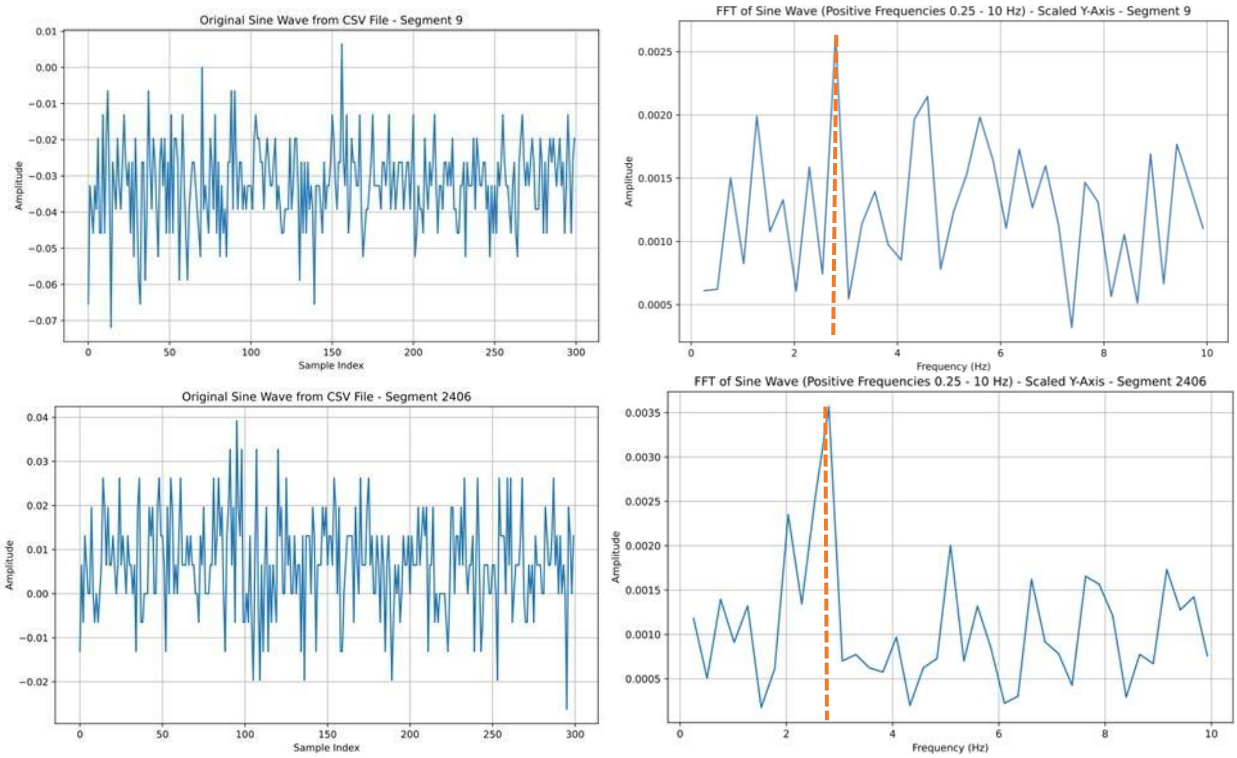

Figure 47. Graphs. Baseline acceleration samples with STFT outputs showing agreement with brake test results.

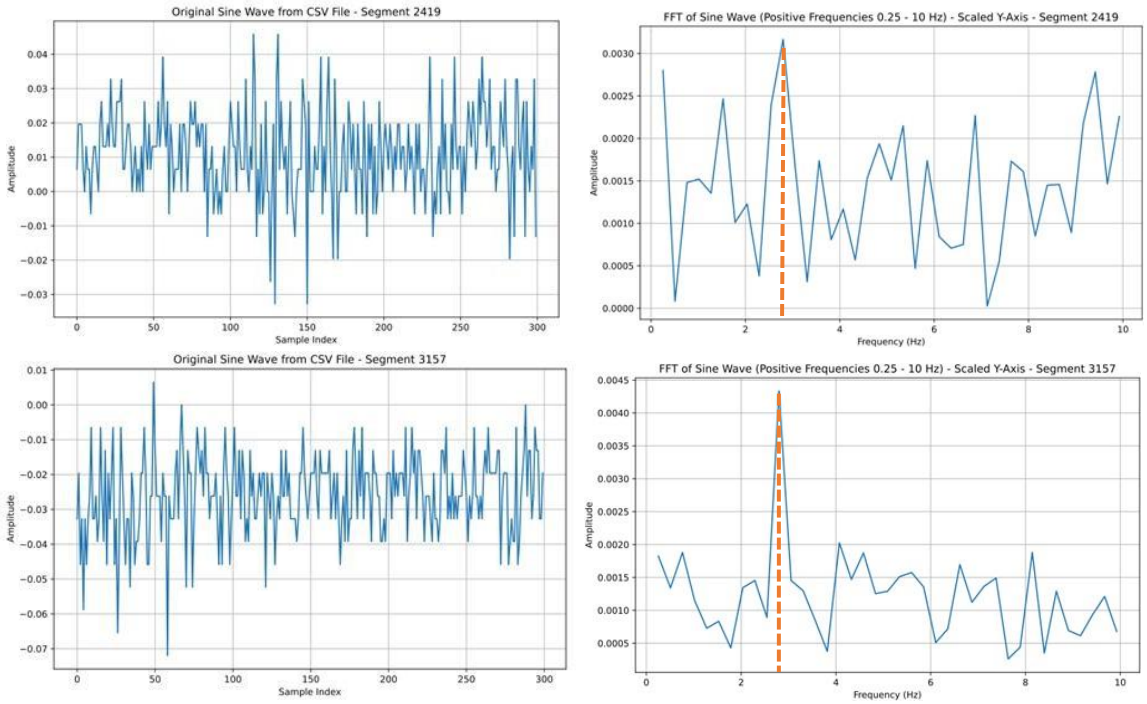

Figure 48. Graphs. No-flooding conditions acceleration samples with STFT outputs with dominant frequency in agreement to brake test result.

High-Flow Data: Flood Event 1 (January 8, 2024)

The first major flood occurred on January 8, 2024, impacting both bridge sites. Validation was provided by upstream hydrograph data and local water-level probes (see figure 49). This event offered the first opportunity to correlate scour depth measurements with changes in bridge vibrational frequency.

Figure 49. Graph. Flooding hydrograph, January 8, 2024.

At Bridge 1, STFT analysis of vibration data revealed a 7.8 percent reduction in natural frequency, from 2.739 to 2.521 Hz (see figure 50).

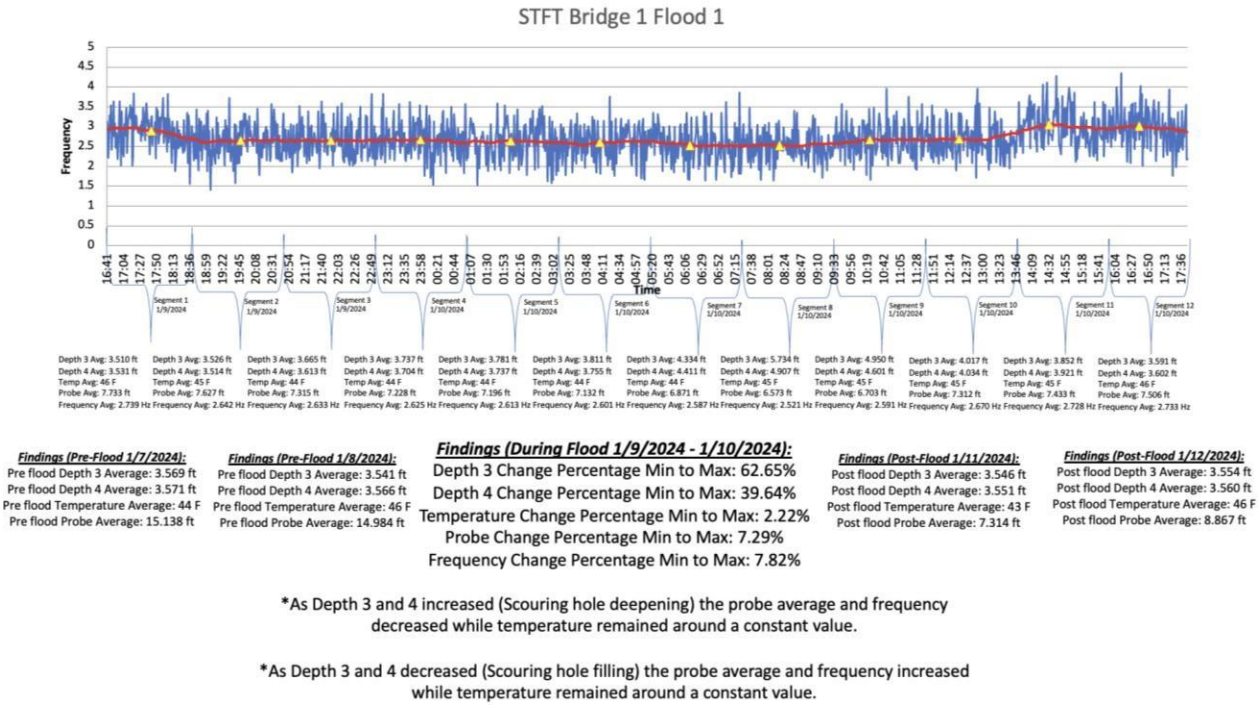

Figure 50. Graph. Output STFT plot, Bridge 1, Flood 1.

Concurrently, sonar depth measurements indicated scour progression: the upstream sensor (Depth 3) recorded an increase from 3.6 to ~6.0 ft, and the leeward sensor (Depth 4) showed

~1.5 ft of scour (see figure 51). Trends demonstrated that frequency decreased as scour deepened and rebounded as sediment refilled.

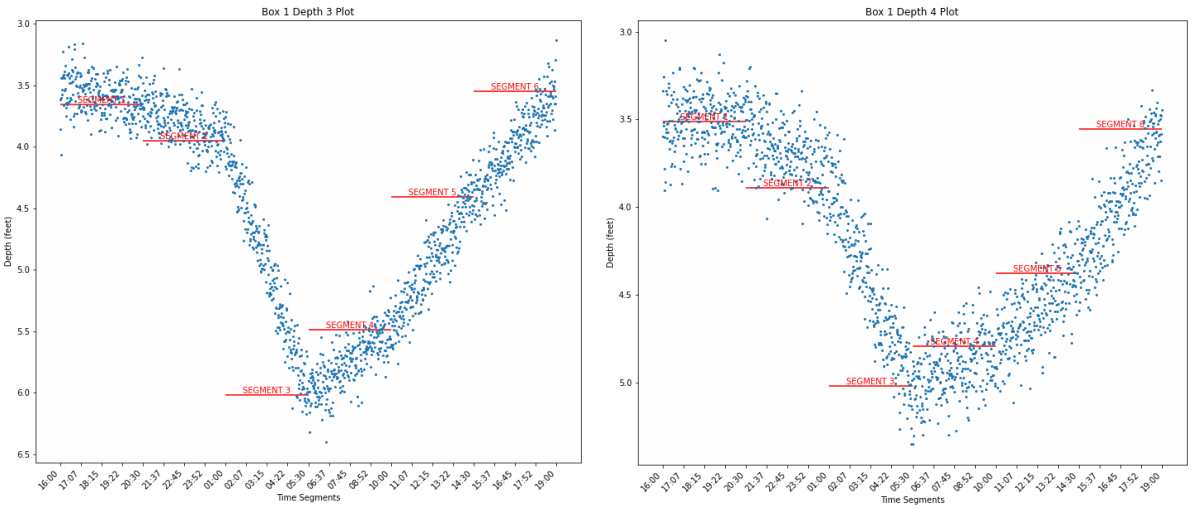

Figure 51. Plots. Scour depth output plots, Depths 3 and 4, Bridge 1, Flood 1.

A comparison with the Colorado State University (CSU) pier scour used the following equation:

$$y_s = 2.0K_1K_2K_3K_4a^{0.65}y_1^{0.35}Fr_1^{0.43} \quad (18)$$

Where,

y_s = Scour depth in feet.

K_1 = Correction factor for pier nose shape.

K_2 = Correction factor for angle of attack of flow.

K_3 = Correction factor for bed condition.

K_4 = Correction factor for armoring of bed material.

a = Pier width in feet.

y_1 = Flow depth directly upstream of the pier. This is taken from the flow distribution output for the cross section just upstream from the bridge.

Fr_1= Froude number directly upstream of the pier. This is taken from the flow distribution output for the cross section just upstream from the bridge.

This comparison showed underprediction of actual scour depth. Whereas the sensors measured ~2.4 ft of scour, the CSU equation estimated only 1.48 ft (see table 8), reflecting limitations of empirical methods in cohesive or complex riverbed conditions.

Table 8. Calculated vs. measured data using CSU formula, Flood 1.

Bridge 1 Flood 1	Collected Data Estimate using CSU	Actual Measurement with Probe
K_1	1.1	N/A
K_2	1.0	N/A
K_3	1.1	N/A
K_4	1.0	N/A
a	1	N/A
y_1	14.25	N/A
Fr_1	0.256	N/A
y_s (Scour Depth)	1.48 ft	2.4 ft

At Bridge 2, Flood 1 scour depths ranged from 0.69 to 1.71 ft across the four sensors (see figure 52 and figure 53).

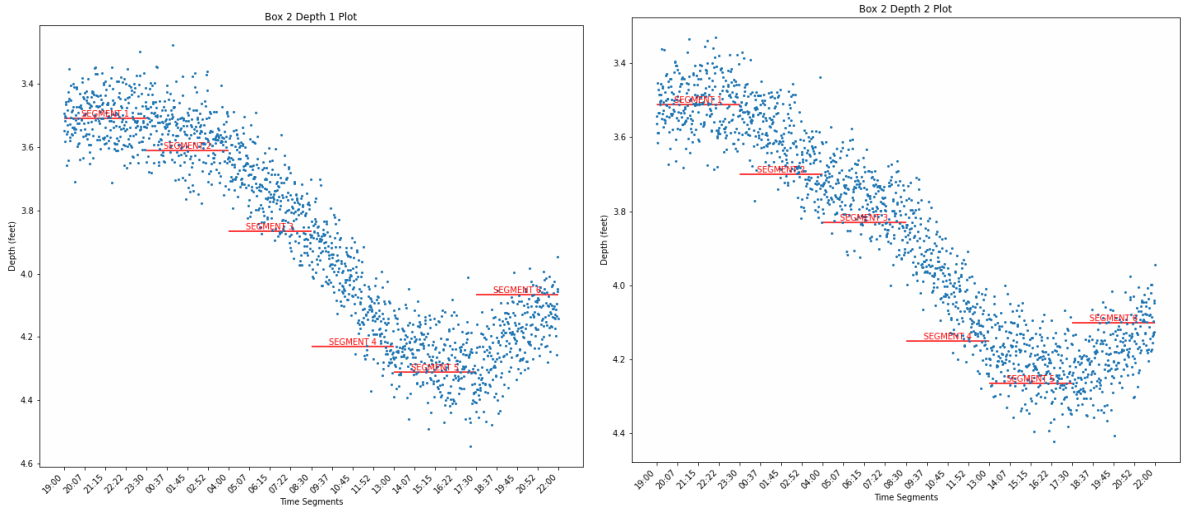

Figure 52. Plots. Scour depth output plots, Depths 1 and 2, Bridge 2, Flood 1.

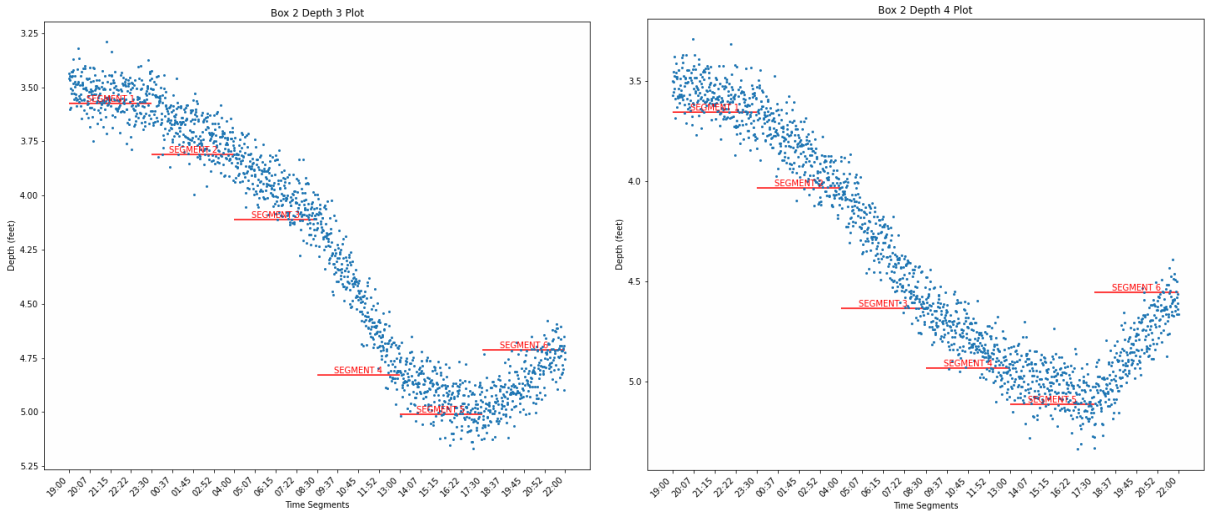

Figure 53. Plots. Scour depth output plots, Depths 3 and 4, Bridge 2, Flood 1.

Vibrational frequency decreased by 0.131 Hz, following the same inverse relationship with scour progression observed at Bridge 1 (see figure 54).

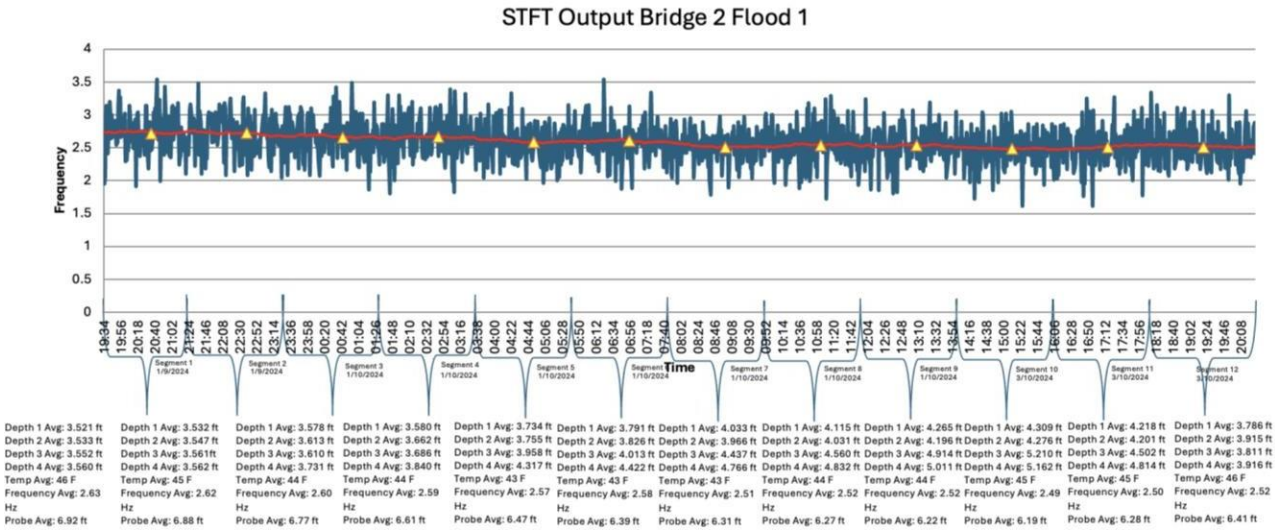

Figure 54. Graph. Output STFT plot, Bridge 2, Flood 1.

High-Flow Data: Flood Event 2 (February 12, 2024)

The second major flood occurred on February 12, 2024. It was smaller in magnitude but still significant, as confirmed by hydrograph and probe data (see figure 55).

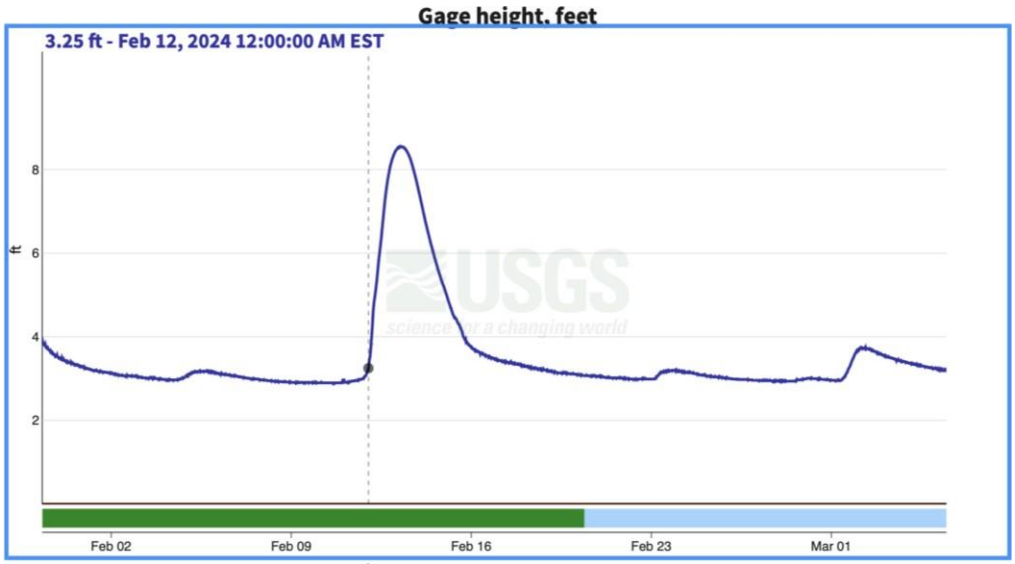

Figure 55. Graph. Flooding hydrograph, February 12, 2024.

At Bridge 1, sonar data showed ~0.85 ft of scour at the upstream sensor (Depth 3) and ~0.10 ft at Depth 4. Frequency decreased by 0.06 Hz (see figure 56), again tracking scour depth progression (see figure 57). CSU equation estimates again underestimated actual scour depths (see table 9).

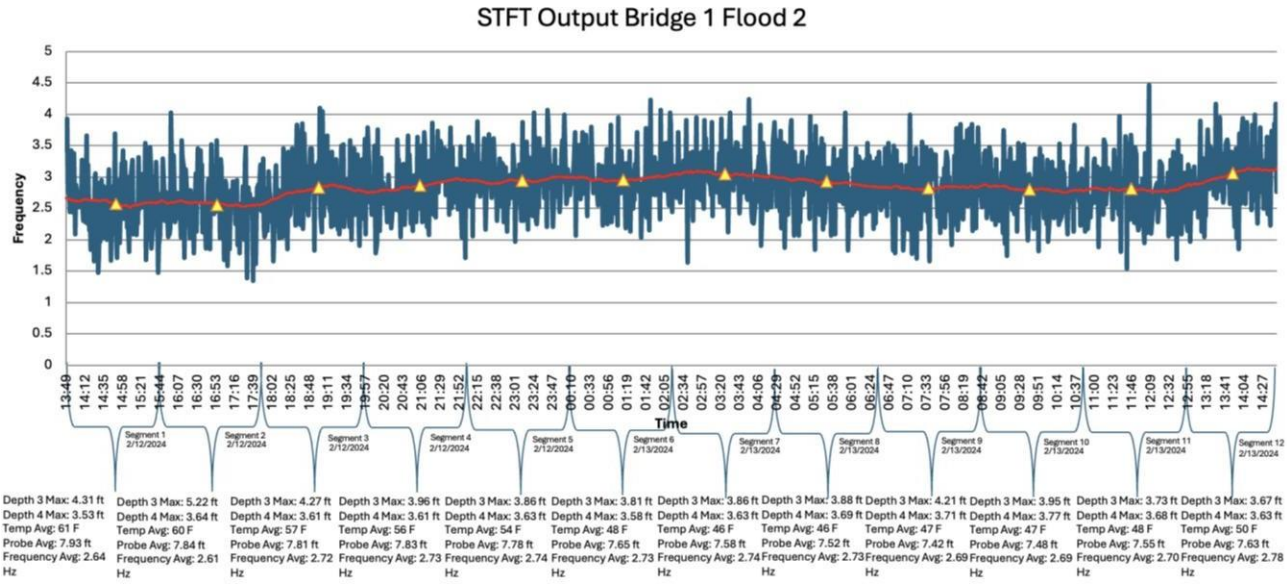

Figure 56. Graph. Output STFT plot, Bridge 1, Flood 2.

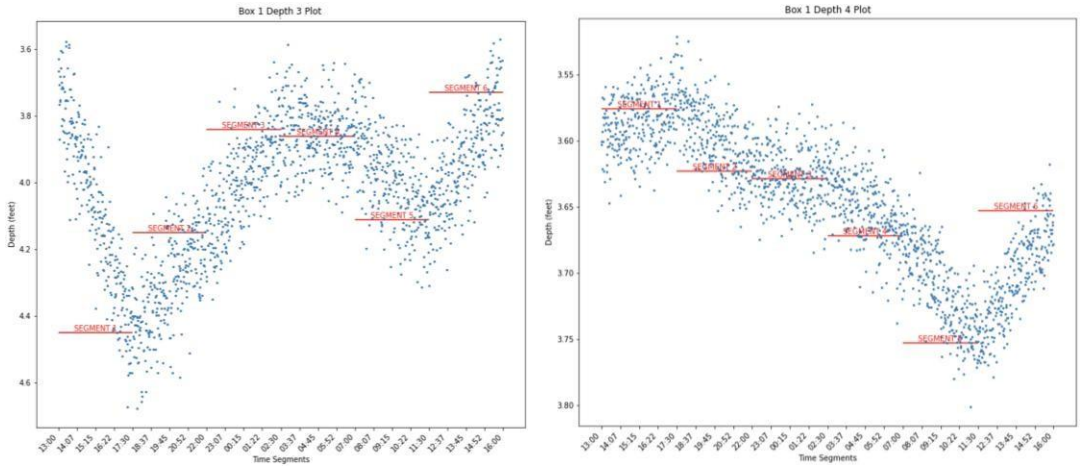

Figure 57. Plots. Scour depth output plots, Depths 3 and 4, Bridge 1, Flood 2.

Table 9. Calculated vs. measured data using CSU formula, Flood 2.

Box 1 Flood 2	Collected Data Estimate using CSU	Actual Measurement with Probe
K_1	1.1	N/A
K_2	1.0	N/A
K_3	1.1	N/A
K_4	1.0	N/A
a	1	N/A
y_1	13.95	N/A
Fr_1	0.259	N/A
y_s [Scour Depth]	1.49 ft	1.55 ft

At Bridge 2, recorded scour depths ranged from 0.53 to 2.09 ft across the four sensors, with a corresponding 0.19 Hz drop in frequency (see figure 58–figure 60). Once again, frequency rebounded as scour holes refilled.

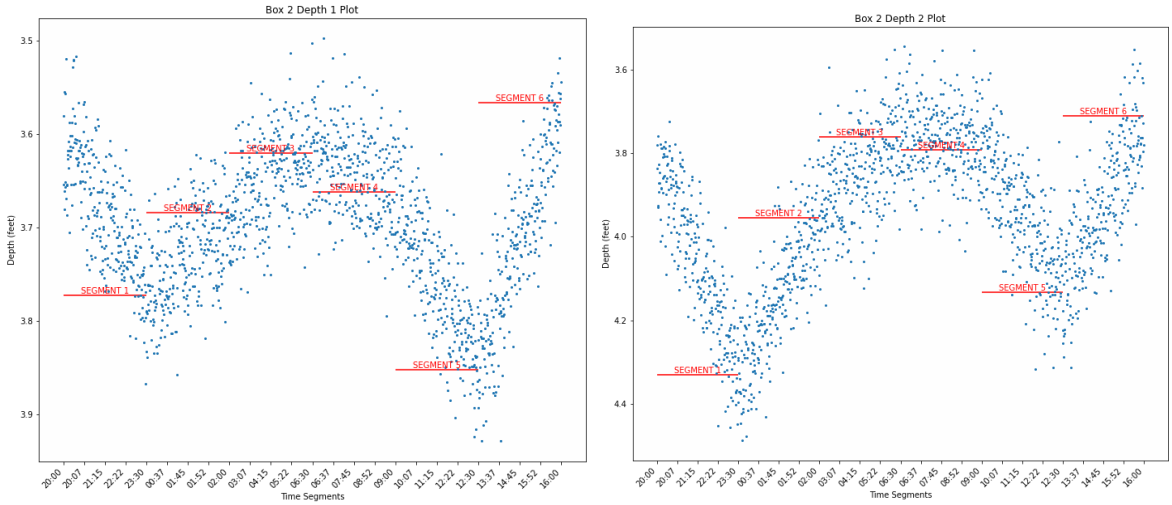

Figure 58. Plots. Scour depth output plots, Depths 1 and 2, Bridge 2, Flood 2.

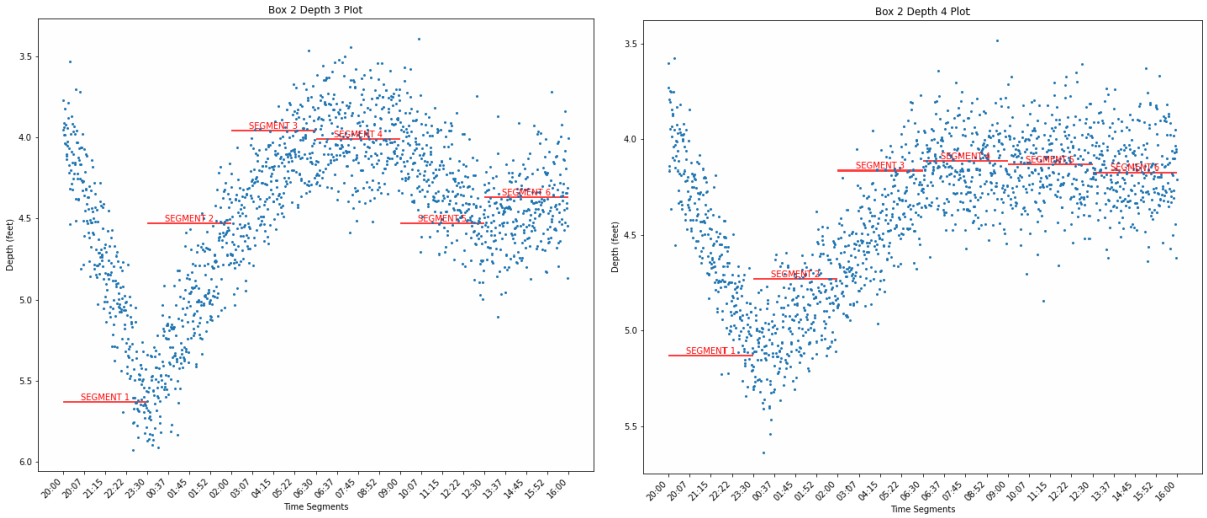

Figure 59. Graph. Scour depth output plots, Depths 3 and 4, Bridge 2, Flood 2.

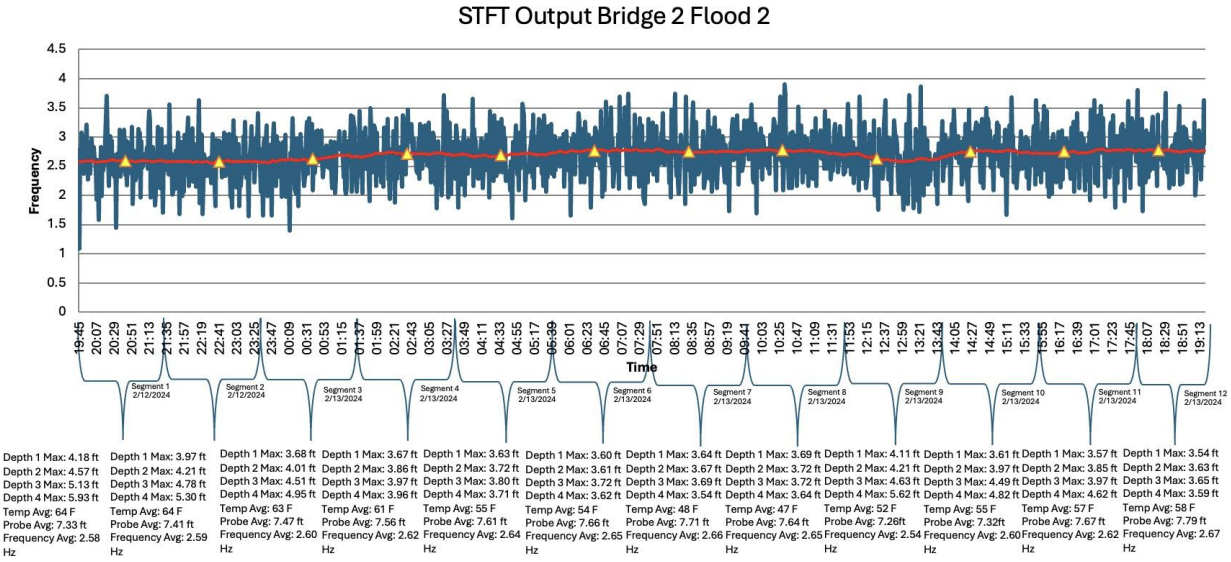

Figure 60. Graph. Output STFT plot, Bridge 2, Flood 2.

High-Flow Data: Flood Event 3 (March 8, 2024)

A third flood occurred on March 8, 2024, comparable in magnitude to Flood 2 (see figure 61).

Figure 61. Graph. Flooding hydrograph, March 8, 2024.

At Bridge 1, Depth 1 recorded 1.09 ft of scour, Depth 2 recorded 0.32 ft, and Depth 4 recorded 0.25 ft; Depth 3 failed during the event. Frequency decreased by 0.22 Hz (see figure 62–figure 64). CSU estimates again underpredicted actual scour depth but showed reasonable correlation (see table 10).

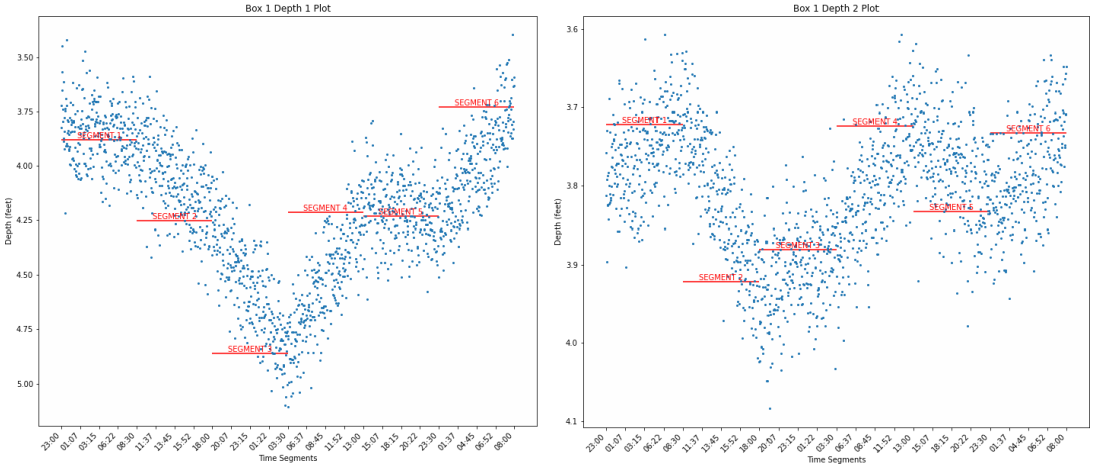

Figure 62. Plots. Scour depth output plots, Depths 1 and 2, Bridge 1, Flood 3.

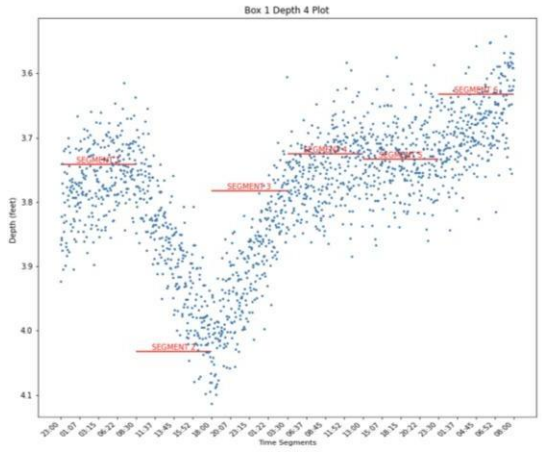

Figure 63. Plot. Scour depth output plot, Depth 4, Bridge 1, Flood 3.

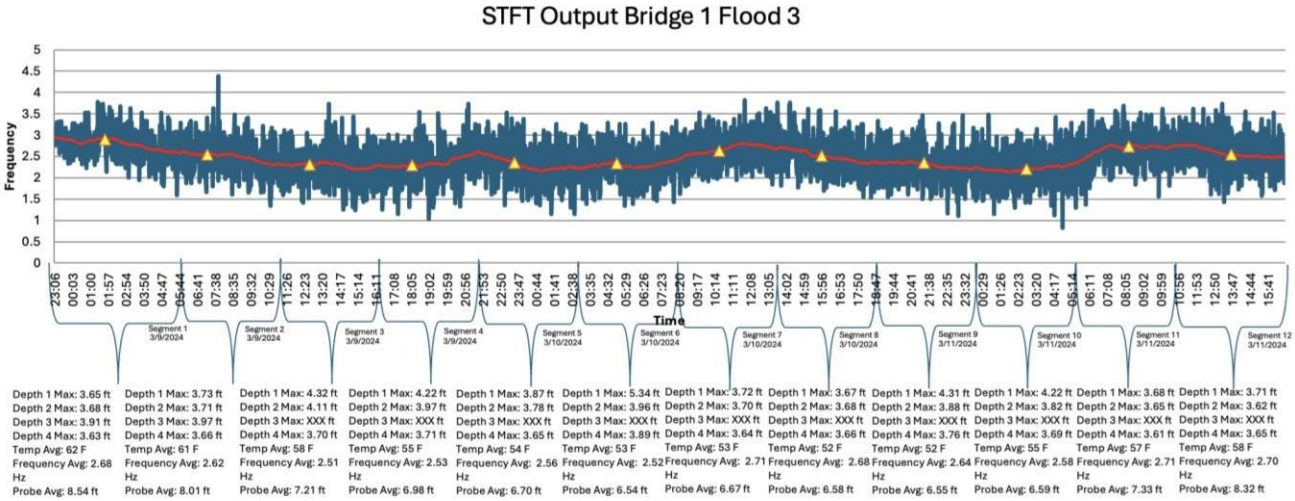

Figure 64. Graph. Output STFT plot, Bridge 1, Flood 3.

Table 10. Calculated vs. measured data using CSU formula, Flood 3.

Box 1 Flood 3	Collected Data Estimate using CSU	Actual Measurement with Probe
K_1	1.1	
K_2	1.0	
K_3	1.1	
K_4	1.0	
a	1	
y_1	13.71	
Fr_1	0.261	
y_s [Scour Depth]	1.50 ft	1.7 ft

At Bridge 2, Depths 1–4 recorded scour depths ranging from 0.22 to 1.2 ft, with frequency decreasing by 0.10 Hz (see figure 65–figure 67).

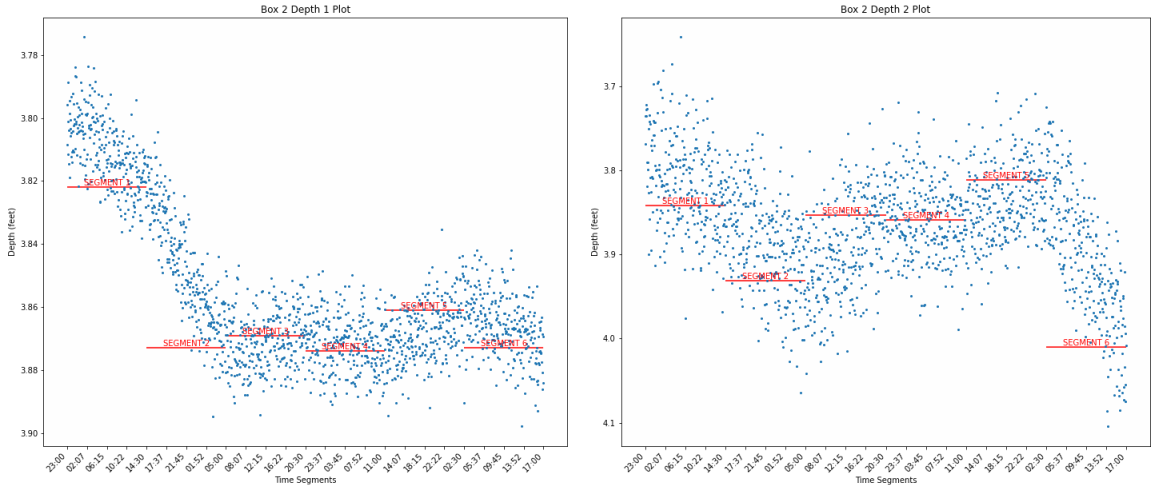

Figure 65. Plots. Scour depth output plots, Depths 1 and 2, Bridge 2, Flood 3.

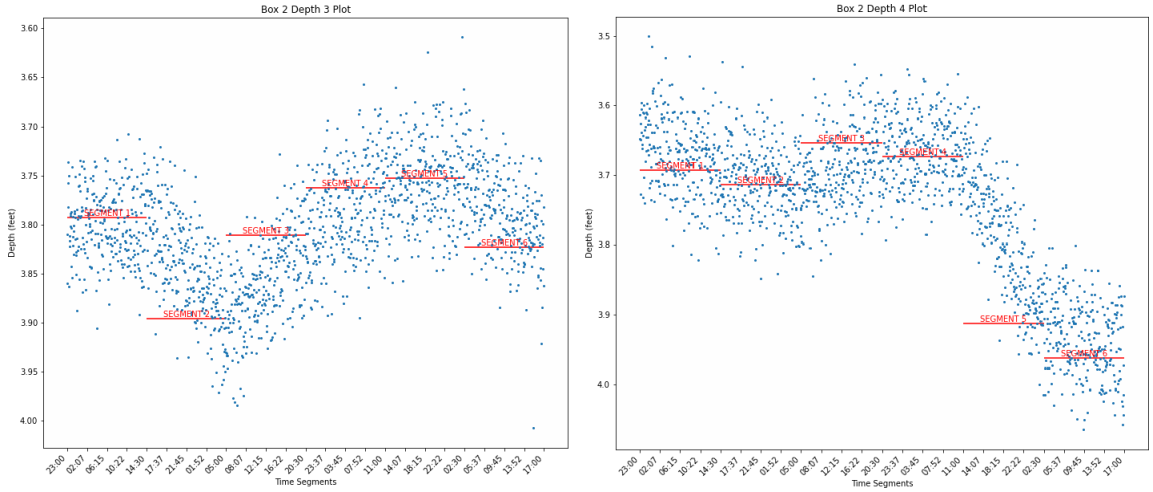

Figure 66. Plots. Scour depth output plots, Depths 3 and 4, Bridge 2, Flood 3.

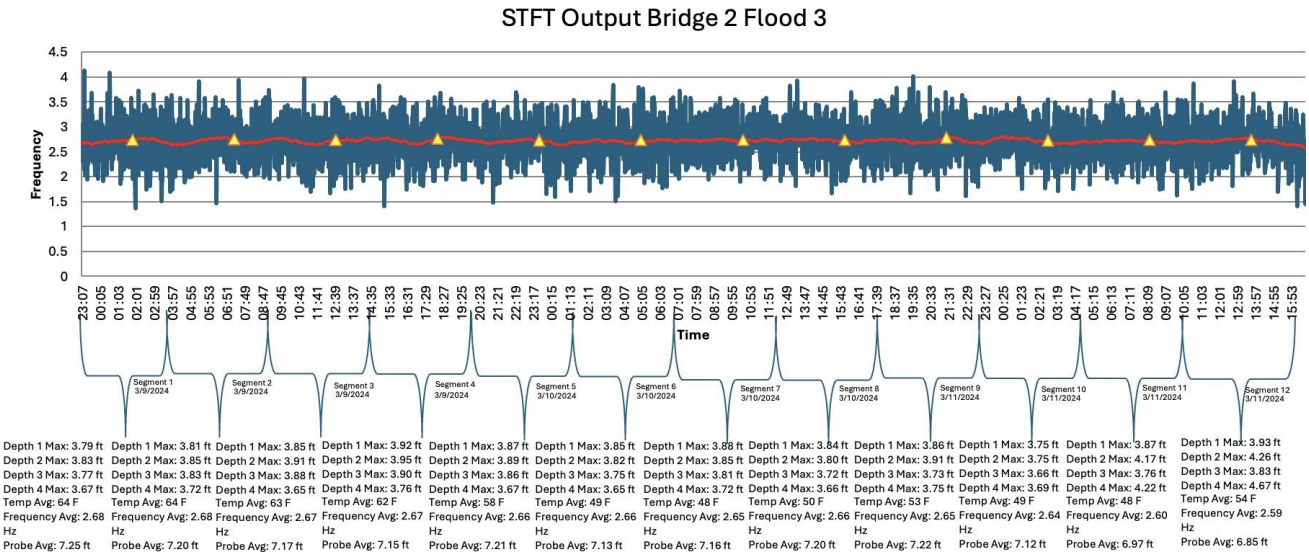

Figure 67. Graph. Output STFT plot, Bridge 2, Flood 3.

Analysis of the three storms brought to light the complexity of the scouring process. With each storm, the calculated Froude Number is similar however the measured scour depths differ. This also indicates that the widely used CSU equation may not necessarily always capture scour depths accurately. Additionally, the bridge vibration characteristics change with the scour depths, even for storms of similar magnitude.

CHAPTER 11. CONCLUSION AND RECOMMENDATIONS

CONCLUSION

Scour monitoring is a critical aspect of infrastructure maintenance and bridge safety. Early detection of excessive scour provides DOTs with the time needed to deploy countermeasures and implement rehabilitation strategies. This is particularly vital during floods and storms, when elevated flows may simultaneously impact numerous scour critical bridges. In such conditions, the absence of reliable scour information not only threatens bridge safety but also places inspectors at risk.

This research addressed these challenges by developing a low-cost (under $1,000) remote bridge scour monitoring system that integrates cost-effective sensors with ML techniques. Two fully functional systems were successfully deployed in the field and demonstrated the ability to collect and transmit data to a cloud-based web server. The system supports two real-time monitoring modes—low-flow and high-flow—enabling continuous observation across a range of hydraulic conditions.

Vibration data captured by the sensors are processed using ML models, which are capable of detecting anomalies during low-flow conditions and estimating scour depths during high-flow events. By combining these model outputs with direct sonar depth measurements, the system is able to issue automated warnings when extreme scour activity is detected.

A supporting web interface, Scour View, was also developed to provide visualization, remote control, and integration with existing GDOT warning systems. In addition to displaying live sensor data, Scour View allows authorized personnel to trigger rapid data collection, review alerts from BridgeWatch©, and plan response strategies. The system is further equipped with

tools for optimizing team allocation during storm events, which can improve operational efficiency during emergencies.

The field deployments confirmed the viability of the system but also highlighted several limitations. Harsh flood conditions and debris can damage scour sensors mounted to bridge bents, and reliance on solar power may be constrained by seasonal canopy cover or site conditions. The current design also lacks integrated measurements of river flow velocity, which are critical for understanding scour dynamics. Instead, flow data had to be inferred from prior hydraulic models, which may not accurately represent changing riverbed and cross-section conditions over time.

Despite these challenges, the research demonstrated the feasibility and effectiveness of a low-cost, real-time scour monitoring system. The integration of field sensors, ML models, and a web-based operational interface offers a scalable solution to enhance bridge safety and resilience during extreme hydrologic events.

RECOMMENDATIONS

Several opportunities exist to further improve the system and expand its capabilities.

- First, deployment should be extended beyond the two test sites to include bridges in diverse hydrologic and geologic settings. Expanding the number of monitored sites will provide a larger and more representative dataset, particularly during flood events, which is essential for refining and validating the ML models. More widespread field deployment would also help confirm the scalability and reliability of the system across varying conditions.

- In terms of sensing capabilities, future iterations of the system could benefit from the addition of cameras to capture supplementary information such as traffic loading or visual evidence of streams' velocities during floods. Integrating flow and velocity sensors would also provide a more complete picture of scour processes and reduce reliance on prior hydraulic models, which may not always reflect current riverbed or cross-sectional conditions.
- From a data processing perspective, improvements in filtering techniques would help mitigate the effects of sensor noise and erroneous reading. Incorporating redundant sensing elements could further strengthen the reliability of the system by ensuring continuous data collection even if individual sensors malfunction or generate anomalous outputs.
- On the ML front, future research should focus on developing anomaly characterization models that can distinguish between different causes of abnormal signals, such as scour, debris impacts, or sensor malfunctions. Additionally, deploying computationally efficient models on edge devices located at bridge sites would enable autonomous, real-time monitoring while reducing reliance on continuous cloud communication. Such an approach would increase system resilience and decrease data transmission requirements during storm events.

By pursuing these improvements, the system can evolve into a robust and scalable platform for continuous bridge health monitoring. Such a system will not only enhance safety during floods but also reduce inspection risks, improve emergency response efficiency, and support long-term resilience of critical infrastructure assets.

ACKNOWLEDGMENTS

Kennesaw State University gratefully acknowledges the financial support for this work provided by the Georgia Department of Transportation (GDOT). We extend our utmost gratitude to Mr. Donn Digamon, State Bridge Engineer, for his support of this project. We also express our sincere appreciation to Mr. Rabindra Koirala, State Bridge Maintenance Engineer, and Mr. Toan Nguyen, Bridge Design Group Leader, Sr., for their thoughtful and valuable insights, which greatly strengthened the project. We further thank GDOT's Bridge Design and Maintenance Office for their assistance during field work, and especially acknowledge the contributions of Mr. Michael Banks and Mr. Matthew Owens, whose input during sensor installation was invaluable. Finally, the research team would like to recognize Ms. Kamari Jordan, Project Manager at the Office of Performance-based Management and Research, for her outstanding guidance and leadership. Her management was instrumental in ensuring the smooth progression and successful completion of this project.

REFERENCES

Briaud, J.-L., Hurlebaus, S., Chang, K.-A., Yao, C., Sharma, H., Yu, O.-Y., Darby, C., Hunt, B.E., and Price, G.R. (2011). *Realtime Monitoring of Bridge Scour Using Remote Monitoring Technology*. Report 0-6060-1, Texas Transportation Institute, College Station, TX. Available online: https://static.tti.tamu.edu/tti.tamu.edu/documents/0-6060-1.pdf.

Computers and Structures, Inc. (2023). *SAP2000 Integrated Software for Structural Analysis and Design: User's Manual*. Version 25, Computers and Structures, Inc.

Curtis, R., Flora, K., Bischoff, J., Marz, R., Cavalier, S., Nassif, H., and Cheng, X. (2017). *Bridge Scour Risk Management*. Project 20 68A, National Cooperative Highway Research Program (NCHRP). Available online: https://onlinepubs.trb.org/onlinepubs/nchrp/docs/NCHRP20-68A_15-02.pdf.

Idaho Water Science Center. (2020). "Real-Time Bridge Scour Monitoring and Evaluation." (website) U.S. Geological Survey, Feb 10. Available online: https://www.usgs.gov/centers/idaho-water-science-center/science/real-time-bridge-scour-monitoring-and-evaluation

Komarizadehasl, S., Mobaraki, B., Ma, H., Lozano-Galant, J.-A., and Turmo, J. (2021). "Development of a Low-cost System for the Accurate Measurement of Structural Vibrations." *Sensors*, *21*(18), 6191. Available online: https://doi.org/10.3390/s21186191.

Mueller, D.S. (2000). *National Bridge Scour Program—Measuring Scour of the Streambed at Highway Bridges*. FS 107-00, U.S. Department of the Interior, U.S. Geological Survey, Reston, VA. Available online: https://pubs.usgs.gov/fs/2000/0107/report.pdf.

Prendergast, L.J. and Gavin, K. (2014). "A Review of Bridge Scour Monitoring Techniques." *Journal of Rock Mechanics and Geotechnical Engineering*, *6*(2), pp. 138–149. Available online: https://doi.org/10.1016/j.jrmge.2014.01.007.

Scannell, J.P. and Baribault, M.K. (2010). "Georgia DOT's Implementation of BridgeWatch." *Proceedings of the 5th International Conference on Scour and Erosion (ICSE-5)*, pp. 924–930. Available online: https://core.ac.uk/download/pdf/326244146.pdf.

Sturm, T.W., Sotiropoulos, F., Landers, M., Gotvald, T., Lee, S.O., Ge, L, Navarro, R., and Escauriaza, C. (2004). *Laboratory and 3D Numerical Modeling with Field Monitoring of Regional Bridge Scour in Georgia*. Final Report, RP 2002, Georgia Department of Transportation, Atlanta, GA. Available online: https://www.researchgate.net/publication/27526139_Laboratory_and_3D_Numerical_Modeling_with_Field_Monitoring_of_Regional_Bridge_Scour_in_Georgia.